

INVESTIGATING TORSIONAL COMPLIANCE OF FLAPPING WINGS TO MAXIMIZE
THRUST CAPABILITY

By

JUSTIN DANIEL MCINTIRE

A THESIS PRESENTED TO THE GRADUATE SCHOOL
OF THE UNIVERSITY OF FLORIDA IN PARTIAL FULFILLMENT
OF THE REQUIREMENTS FOR THE DEGREE OF
MASTER OF SCIENCE

UNIVERSITY OF FLORIDA

2011

© 2011 Justin Daniel McIntire

To my family and friends who have always believed in my ability to succeed, and have also helped me along the way

ACKNOWLEDGMENTS

I first and foremost thank my parents for always pushing me to do more, and to become a better person. I thank my girlfriend for putting up with me and always supporting me. I also want to thank my professor, Peter Ifju, for allowing me to work under him, for always answering my questions, for helping whenever I asked; for being not only a great professor, but a great person.

TABLE OF CONTENTS

	<u>page</u>
ACKNOWLEDGMENTS.....	4
LIST OF TABLES.....	7
LIST OF FIGURES.....	8
NOMENCLATURE	10
ABSTRACT	11
CHAPTER	
1 INTRODUCTION	13
2 EXPERIMENTAL TECHNIQUES.....	20
2.1 Wing Construction.....	20
2.2 Flapping Mechanisms	21
2.2.1 The FL2D3 Flapping Mechanism.....	21
2.2.2 The FL2D3V2 Flapping Mechanism	23
2.2.3 The Geared Flapping Mechanism	24
2.3 Force Sensor	25
2.4 Digital Image Correlation	25
2.4.1 Camera and Lens Selection	26
2.4.2 Experimental Setup	27
2.4.3 DIC Procedure.....	28
2.4.4 Stroboscope and Trigger Timing	30
3 ANALYSIS TECHNIQUES.....	32
3.1 Main Hypothesis	32
3.2 Post Processing of DIC Data	33
3.3 Selected Variables for Analysis	35
3.3.1 Twist at Span-wise Locations	35
3.3.2 Enclosed Volume and its Centroid.....	36
3.3.3 Twist Volume and its Centroid.....	42
3.4 DIC Data Analyzed Using the Selected Variables.....	43
3.5 FE Model of the Wing	47
3.5.1 Justification for FE Model	47
3.5.2 Reason for the Selection of Mid-plane for the Model.....	47
3.5.3 Explicit vs. Implicit Analysis	48
3.5.4 FE Model Setup.....	49
3.5.5 Load and Boundary Conditions	51
3.5.6 Adjustment of the Magnitude of the Distributed Load	52

3.5.7 Advantage for the FE model	54
3.6 Candidates for Increased Thrust.....	55
3.7 High Speed Camera Analysis	56
4 RESULTS AND DISCUSSION	59
4.1 Visual Comparison of DIC Data and Model Output.....	59
4.2 Tested Wing Designs.....	61
4.3 Model Results	62
4.4 Build and Test of Modeled Wings	64
5 CONCLUSIONS AND FUTURE WORK	66
LIST OF REFERENCES	68
BIOGRAPHICAL SKETCH.....	70

LIST OF TABLES

<u>Table</u>		<u>page</u>
3-1	List of sections used in the finite element model	50
3-2	List of the final λ used, the average error, and the magnitude of the load for each frequency	54

LIST OF FIGURES

<u>Figure</u>	<u>page</u>
1-1 Pin Wu's wing study with varying stiffness.....	16
1-2 Wings with varying structural stiffness graphed with the flapping frequency vs. the average thrust production	17
1-3 Wing tip deflection and twist were graphed vs. flap angle for different wing structures.....	17
2-1 Example layout of wing.....	20
2-2 FL2D3 flapping mechanism.....	22
2-3 FL2D3V2 flapping mechanism.....	23
2-4 The geared flapping mechanism.	24
2-5 The experimental setup	26
3-1 Visual comparison of wing rotating through a single degree of freedom flap angle θ	32
3-2 How the wing is rotated and translated.....	34
3-3 How the wing is further transformed.	35
3-4 Twist is measured at different percentages of the total span, at each of the lines shown.....	36
3-5 A depiction of the enclosed volume under the wing, and its centroid.	37
3-6 Wing divided into boxes outlined in blue, and their centroid is shown with a green dot	38
3-7 Volume and centroid vs. box size.....	39
3-8 Graph of chosen box size vs. elapsed time to calculate enclosed volume.	39
3-9 Comparison graphs between quad2d integration and 4 corner average techniques.....	40
3-10 Comparison graphs between quad2d integration and 4 corner average techniques.....	40
3-11 A visual reason for the divergence of the X centroid using the averaging method	41

3-12	Figure depicting the twist enclosed volume, and its centroid.....	42
3-13	The three preliminary wings chosen for the post DIC analysis are shown above.....	43
3-14	The displacement of the X centroid vs. thrust.....	44
3-15	The displacement of the Z centroid vs. thrust.....	45
3-16	The movement of the centroid in the X-Z plane as twisting deformation increases	46
3-17	The change in enclosed twist volume vs. thrust.	47
3-18	This is the angular position, velocity, and acceleration, at the wing mount of the current flapper	48
3-19	The wrinkling in the Capran membrane can be seen in this figure. Due to the irregular shaped elements, the implicit solver fails to converge	49
3-20	This is the distribution of the applied aerodynamic loading, used in Abaqus.....	51
3-21	Graph of the adjusted error to a given lambda λ for the three wings at 15Hz.....	54
3-22	Image sequence of shockwave going through the trailing edge of a perimeter reinforced wing without rigid root attachment.	57
4-1	A visual comparison between the DIC images at mid-plane (left) and the model output (right)	60
4-2	A lineup of a set of wings tested in the Abaqus code	61
4-3	The movement of the centroid was compared for all designed wings against each other and the preliminary wings for all frequencies.....	62
4-4	The amount of enclosed twist volume was compared for all designed wings against each other and the preliminary wings for all frequencies	63
4-5	Shown above is the old wing 5, and the modification made to make it stiffer.	64
4-6	This is a graph of measured thrust vs. frequency for the 4 wings built from the model, as well as the modified wing 5	65

NOMENCLATURE

MAV	Abbreviation for Micro Air Vehicle
DIC	Abbreviation for Digital Image Correlation, a non-contact method for measuring 3-dimensional deformation using a set of set of stereo digital cameras and imaging software
FEA	Finite Element Analysis
α_{25}	Twist chord-wise at 25% of the current span
α_{50}	Twist chord-wise at 50% of the current span
α_{75}	Twist chord-wise at 75% of the current span
b	wing span
c	chord
L	Average lift produced by current wing
T	Average thrust produced by current wing
V	enclosed volume of the deformed wing
V_{twist}	enclosed twist volume of the deformed wing
X_c	X centroid of the enclosed volume (along the chord)
Y_c	Y centroid of the enclosed volume (along the span)
Z_c	Z centroid of the enclosed volume (out of plane)
ω	Frequency of flapping in Hz
θ	Flap angle of wing
u, v, w	Cartesian displacements
x, y, z	Cartesian coordinates

Abstract of Thesis Presented to the Graduate School
of the University of Florida in Partial Fulfillment of the
Requirements for the Master of Science

INVESTIGATING TORSIONAL COMPLIANCE OF FLAPPING WINGS TO MAXIMIZE
THRUST CAPABILITY

By

Justin Daniel McIntire

December 2011

Chair: Peter Ifju
Major: Mechanical Engineering

This work involves maximizing the thrust capability of small flapping wings. The motivation of this work is to create a wing with a particular architecture to allow it to passively deform from going through a single degree of freedom flapping motion, to create the largest amount of thrust. The main hypothesis was that increased twist about the leading edge produces more thrust.

Carbon fiber wing skeletons measuring approximately 75mm X 25mm were created with various layouts, and then were adhered to a thin membrane. They were then attached to a flapping device mounted on top of a force sensor, and the wings were tested at different flapping frequencies, while thrust values were obtained. Digital image correlation was also performed while the wings were in motion to acquire the deformation data throughout the flap cycle.

A finite element model was also created to try and mimic the wing at a particular point in the flap cycle. The loads were determined by comparison to the previously obtained digital image correlation data. With this model, new wing geometries could be tested at various loads without the need to physically construct the wing. This equated approximately to a time cost savings of 16 times that of actual construction.

To determine if a wing was a better candidate for increased thrust, the twist about the leading edge had to have increased over previously tested wings. The finite element model did find designs with increased torsional capability, but direct construction of these layouts resulted in higher thrust values only at lower frequencies. After some slight modifications to the designs to stiffen them at higher frequencies, wings were achieved with over a 18% improvement over any previous designs.

CHAPTER 1 INTRODUCTION

Powered flying machines have been around for over a century. Great leaps in aviation have led to the design of not only airplanes, but helicopters and even space ships, yet in the beginning the inspiration came from nature. Even the great inventor Leonardo da Vinci, the conceptual inventor of the helicopter, was motivated by flapping flight of animals. Looking back on his time, one could say that he was inspired because this was all he knew that could fly, but even the same man today would still see that flapping flights' incredible ability to hover and maneuver in tight spaces far exceeds anything else that mankind has yet been able to come up with.¹² It is this reason that motivates researchers to create flying machines using flapping wings.

Micro air vehicles (MAV's) are defined as aerial robots with a maximum physical dimension of 15 cm or less.¹⁰ It is specifically in this category where flapping wings are desirable, not only due to their increased ability to maneuver delicately, but because at low Reynolds Numbers a flapping wing propulsion system is more efficient than a conventional rotational propeller.⁷ Also, at this point in time, a MAV's primary purpose is in surveillance, which requires the slow flight and agility that a flapping wing system can produce.¹³

But there are only a few such flying machines in the world today due to the complex makeup of flapping flight, and the lack of research on comparable devices in nature. Research about flapping insects, on subjects such as wing attitude during flapping, structural morphology of a wing, and the action of indirect wing muscles are very sparse,¹⁴ but some things are known. The traditional approach of aerodynamic force production, or the 'quasi-steady' theory, only describes a portion of the thrust

produced by insect wings. It is shown by Mao Sun that even the maximum coefficient of lift generated by a fruit fly's wings is not enough to support its weight, and this is the case for many other insects.⁴ It is unsteady aerodynamic forces which make the flight of many of these insects possible. These force-enhancing phenomena include leading edge vortex generation, which increase the circulation around the wing by effectively increases the camber,⁵ as well as rapid pitch up rotation at the wing reversal, which is in itself a source of circulation.⁶ It is also noted in⁶ that these phenomena are most extreme in animals that use a roughly horizontal stroke plane, such as flies, bees, and hummingbirds, in which hovering flight is largely exploited.

Although the force production in flapping flight is quite complex, one fact stays constant, and that is that twisting about the wing's leading edge is necessary for all forms of thrust production. In 'quasi-steady' theory, the wing must remain at a certain angle of attack to produce a net force. The same is true with unsteady force production. Without a set angle of attack, the leading edge vortex bubble would have no effect due to the fact that force transmission is normal to the wing. Also, it is obvious that twisting is necessary for rapid pitch up rotation. In other words, twisting is paramount to thrust production in flapping wings.

There are different methods employed to create this twisting motion to set the angle of attack during the flapping cycle. Hummingbirds use active control, while some insect wings do this mainly passively, due to the fact that they have no muscular control past the wing base.³ The torsional angles in these insects' wings can be controlled passively by the aerodynamic and inertial changes due to the flapping motion.¹ Specifically, it is controlled primarily by the architecture and material properties of the

wing, which allow beneficial thrust-producing deformations to occur.¹⁵ An example of this is the way that a dragonfly's corrugated wing veins are arranged to increase bending stiffness along the span, and decrease torsional rigidity.²

Although robotic mechanisms do exist to allow active control over multiple degree of freedom flapping,⁸ for a device as small as a MAV, where simplicity and weight savings are a necessity, it is ideal to have a single degree of freedom flapper. With a single degree of freedom, a flexible wing can be used so that passive deformation can occur, with a structure designed to maximize thrust production.¹⁶ This can be done by tailoring the wing to twist along the span when loaded.¹¹ But the torsional stiffness cannot be too high, or too low, it must be at an optimum. If the torsional stiffness is too high, then there is little to no twist, but if the torsional stiffness is too low the wing is too compliant, and the angle of attack goes to zero.⁹ Either extreme ends in little to no thrust production, so a balance must be found.

The investigation being done presently has been built upon the work of others. It was found by Pin Wu¹⁶ that deformation during flapping has a significant effect on aerodynamic performance. This deformation was dominated by the stiffness of the wing, and inertia due to its mass. He gathered data from a load cell to get the average thrust output of a wing, and took digital image correlation images to analyze the deformation of that wing. Through experimentation he then succeeded in correlating certain aspects of wing deformation to thrust generation.

One of his most basic, but most powerful findings was the influence of leading edge stiffness on thrust output of a wing. In his study, he created wings with the planform seen in Figure 1-1a, and varied the number of layers of carbon fiber structural

reinforcements for both the leading edge and the batten structures, as seen in Figure 1-1b. His naming scheme was L(#)B(#), with L standing for leading edge, B standing for batten, and # being the number of layers of each of these.

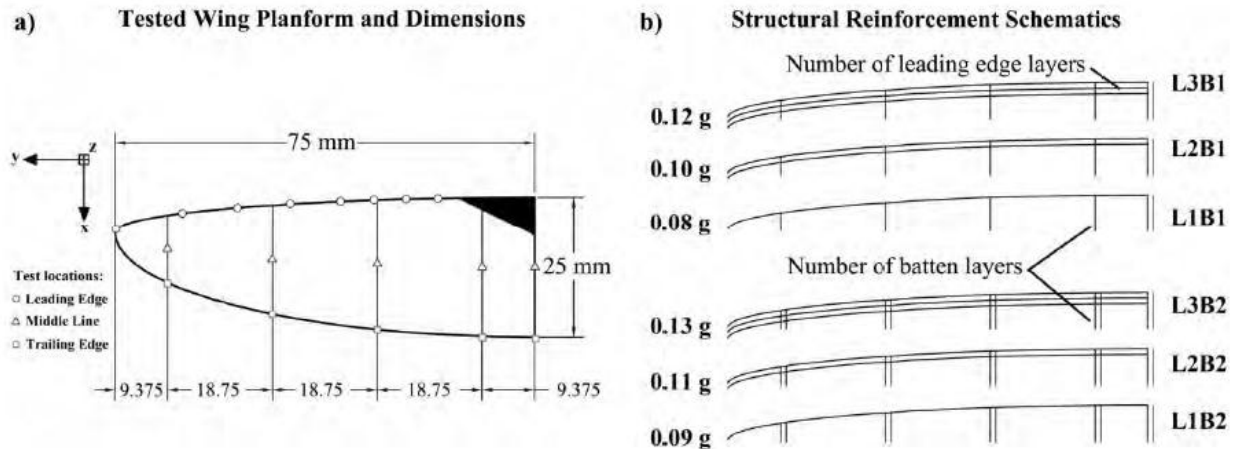


Figure 1-1. Pin Wu's wing study with varying stiffness. A) This is the layout of the wing used in the study. B) This illustrates how the number of layers of carbon fiber were varied to produce different stiffness in the leading edge and battens.

His findings for multiple frequencies are shown in Figure 1-2. The thrust was measured over a constant time period, and the average of this thrust output was found. The stiffness of the leading edge had a very significant effect on the average thrust of the wing. The wings with only one layer of leading edge did relatively poorly. Those with two layers produced the most thrust at modest flapping frequencies, but above 30Hz their thrust output declined. Those with three layers produced the most thrust at maximum frequencies, but did not do as well as the two layer wings at lower frequencies. This study found the profound impact that leading edge stiffness had on thrust production, and how it must be tailored to a certain flap frequency to maximize the thrust potential. Although batten stiffness did have some effect, it was very small in comparison to that of the stiffness of the leading edge.

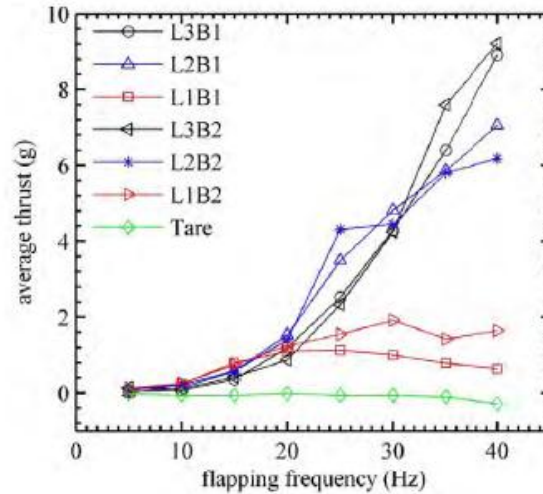


Figure 1-2. Wings with varying structural stiffness graphed with the flapping frequency vs. the average thrust production.

He also found relationships between the tip deflection of the wing and the twist at 75% of the span throughout the flap cycle, to thrust production. By graphing the tip deflection (w_{tip}/c) for all flap angles and wing twist (α_{twist}) for all angles, he found a relationship in the area enclosed by this graph, as well as the phase angle this graph was on. This can be seen in Figure 1-3.

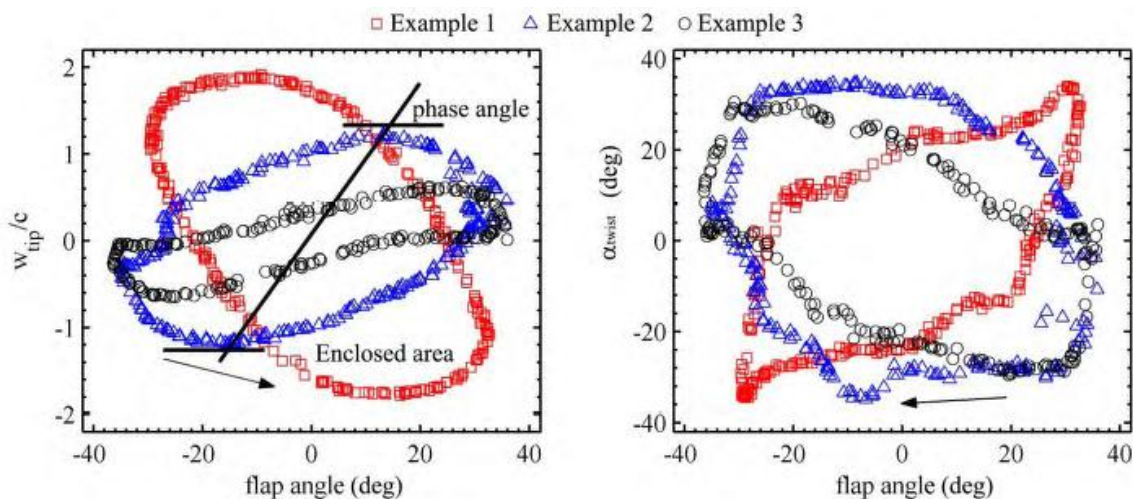


Figure 1-3. Wing tip deflection and twist were graphed vs. flap angle for different wing structures. A positive correlation between enclosed area and thrust was found, as was increasing phase angle and thrust (as long as the phase angle did not pass 90°).

He was able to characterize increased thrust production with regards to certain deformations that the wing experienced during flapping, which was a novel approach. It was found that increasing enclosed area of these graphs could be directly correlated to increased thrust. It was also found that increasing of the phase angle corresponded to increased thrust, unless this angle exceeded 90° (this was found to decrease thrust and was due to excessive compliance). His wing tip deflection was able to describe the bending of the wing, while the twist at 75% of the span was able to describe twist.

These parameters he chose to describe both bending and twisting only described a portion of the full deformation that the wing experienced. The richness of the DIC data and the simplicity of the parameters chosen, fueled future expanded exploration into this collected data. It was his initial experimental exploration into passive deformations which paved the way for the work described in this paper.

The current work involves optimizing the architecture of a flexible wing so that a single degree of freedom flapper produces the most thrust possible. The wing is constructed of a carbon fiber skeleton and adhered to a thin nylon membrane, and measures 75mm at the span and 25mm at the chord. The skeleton itself is what is varied from iteration to iteration, with the final goal being a layout that allows for passive deformation that maximizes thrust production.

A main issue with the construction of these wings was their high time cost for construction, so to facilitate design speed a finite element model was made of the wing with an aerodynamic load mirroring what happened at mid-plane in the flap cycle. Although this model was very elementary due to the fact that it only depicted the wing in one position of the highly dynamic flapping motion, it did give some insight into designs

which are desirable, specifically designs with high torsional compliance. To determine the magnitude of this compliance proved to be quite challenging, due to the complex shapes the deformed wings would take on.

To make describing twist simple, a single variable that made up the enclosed volume between the deformed wing, and its un-deformed counterpart was found. The location of the centroid of this enclosed volume proved to be highly correlated to not only the twist of the wing, but the thrust produced as well. Also, it was found that if this enclosed volume decreased rapidly that this was correlated to too much torsional compliance, and essentially failure of the wing. Using this finite element model, designs were created that were thought to enhance torsional compliance, and were ranked based on the movement of the centroid of the enclosed volume. Using this method, wing architectures which showed little promise were eliminated, while those which excelled were built and tested.

CHAPTER 2
EXPERIMENTAL TECHNIQUES

2.1 Wing Construction

The structure of the wing was chosen to mimic what is seen in nature, specifically that of a hummingbird wing. Each wing (Figure 2-1) was based on an Inverse Zimmerman planform, and had an aspect ratio similar to a hummingbird of 7.65 (75mm span and 25mm chord). This planform was later exchanged with a simpler quarter ellipse, which was desirable due to its ease of construction.

The materials used not only had to withstand the extremely variable aerodynamic and inertial loading, but had to be light enough to be used on a MAV. Carbon fiber of varying thicknesses was used for the skeletal support structure due to its high elastic modulus and low density. This structure was then adhered to a thin nylon film made by Honeywell named CAPRAN® , which was used as the membrane of the wing due to its relatively high tensile strength (28,000-40,000 psi) for its extremely low thickness (14 microns) and therefore low mass. The total mass of most wings resided between 0.12g and 0.22g, depending on the support batten configuration.

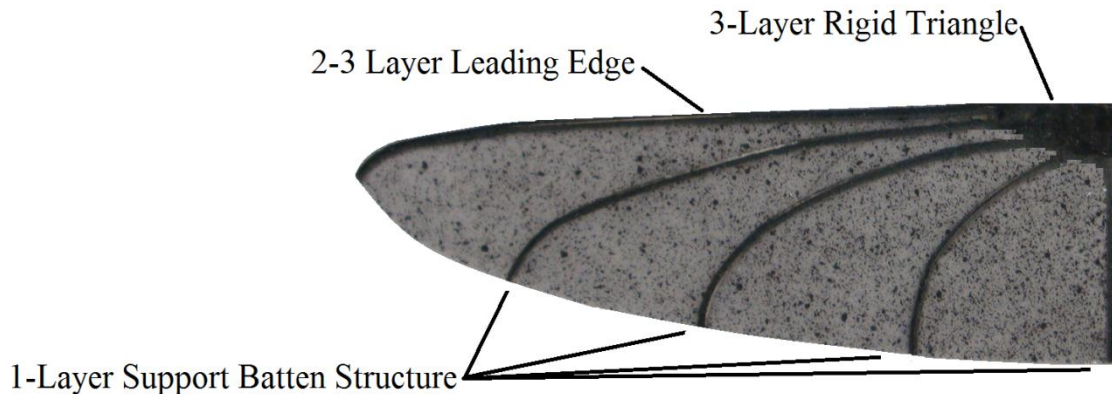


Figure 2-1. Example layout of wing. The wing measures $b = 75\text{mm}$, $c = 25\text{mm}$, and is constructed of a carbon fiber skeleton adhered to a speckled Capran membrane. The wing shown has 4 support battens.

The basic layout for the carbon fiber skeleton began with a rigid triangle made up of 3 layers of bidirectional carbon fiber, measuring 6mm x 12mm. This was the attachment point for the wing onto the flapping mechanism. Sandwiched between those layers was a leading edge made up of 2-3 layers of unidirectional carbon fiber, which measured 0.8mm in width, and ran the entire span of the wing. The support batten structure of the rest of the wing was allowed to be variable, but a batten width of 0.8mm and a thickness of 1 layer of unidirectional carbon fiber, was held constant. A speckle pattern was also applied to one side of the wing so that Digital Image Correlation could be performed.

Adhesive selection. A peel test was performed on samples of carbon fiber and CAPRAN®, attached with varying adhesives, so that the best one could be selected. The samples were placed in an Instron machine, and were pulled apart until failure occurred. Although an adhesive spray named Super 77 performed with the highest tensile strength, it was noticed that it remained “tacky” and slowly peeled away. The second leading candidate, a thin cyanoacrylate adhesive, showed that although its tensile strength was slightly lower, it failed rather abruptly. This behavior was much more desirable because of the highly dynamic forces that occur along the wing, and it was decided that the nearly static tension test’s results did not take this into account. It was for these reasons that the thin cyanoacrylate adhesive was used.

2.2 Flapping Mechanisms

2.2.1 The FL2D3 Flapping Mechanism

The first flapping mechanism used, the FL2D3, was designed and fabricated by a former PHD student, Pin Wu (Figure 2-2). It, and every other flapping mechanism presented, utilized an EC-16 brushless DC Maxon motor

(<http://www.maxonmotorusa.com>), a planetary gearhead that had a 57/13 reduction, and a 256 counts/revolution motor encoder with a EPOS 24 controller. The motor's nominal output was between 0 and 21 N•mm, and it also had the ability to rotate at any frequency from 0 to 45 Hz, which was regulated by the encoder and controller feedback.

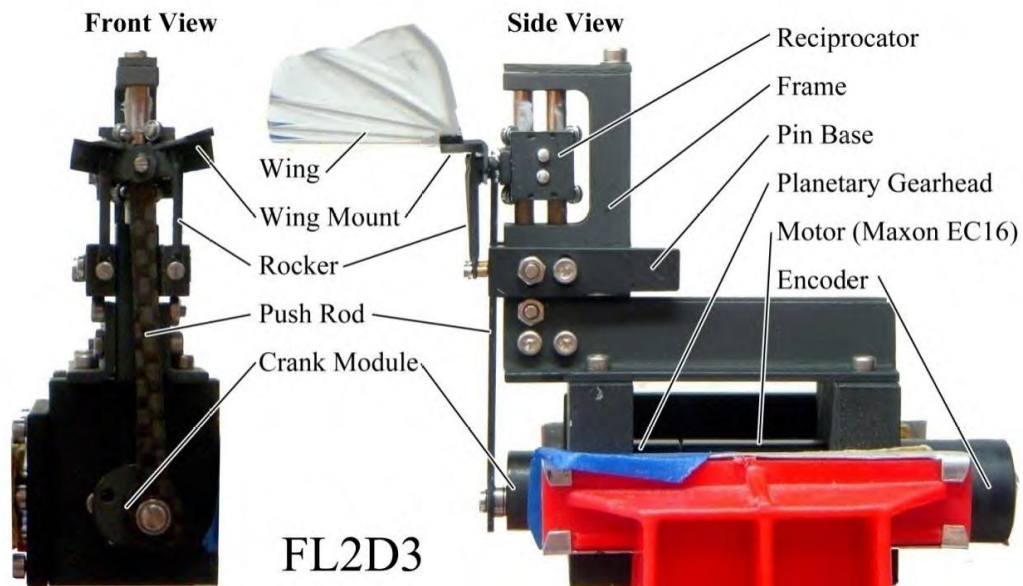


Figure 2-2. FL2D3 flapping mechanism, capable of 45 Hz, $\pm 60^\circ$. Courtesy of Pin Wu.

As with all of the mechanisms presented in this paper, this was a single degree of freedom flapper. The motor's rotational output was converted to linear vertical motion by the push rod and reciprocator combination. The center pin of the reciprocator was then connected to the wing mount, which pivoted about the rocker arm, allowing a simple flapping motion to occur. This flapping mechanism had a nominal flap angle of $\pm 35^\circ$, but was adjustable by changing the attachment point of the push rod on the crank module. The flapper performed its function very well, but the large numbers of connection hardware were undesirable because they tended to loosen with the vibrations that accompany high frequency flapping.

2.2.2 The FL2D3V2 Flapping Mechanism

The FL2D3V2 (Figure 2-3) was an updated version of the previous flapping mechanism. One main difference between it and its predecessor was the replacement of the reciprocator, which before was a total of 12 parts, into a single block of nylon. This decreased complexity, the need for lubrication, as well as the need to constantly tighten screws within the reciprocator portion of the flapper. Nylon was selected for its low density, so that the inertia in the mechanism was kept to a minimum. The handmade rockers were replaced with machined ones, and the wing mounts were replaced with machined aluminum versions with a recessed surface for more consistent wing placement.

The FL2D3V2 was also painted white to help with the data obtained through Digital Image Correlation (DIC). One problem with DIC with the flapping setup was the inability to accurately find the edge of the wing, due to the fact that the battens were a solid black color, the same as the prior version of the flapper. By painting the updated version white, the DIC system was able to find the entire wing more consistently.

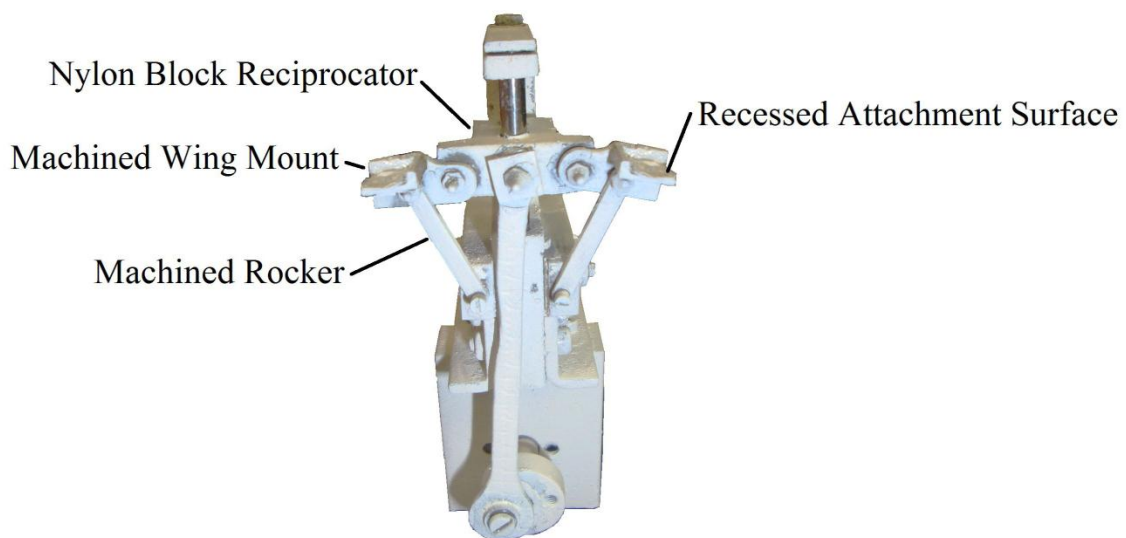


Figure 2-3. FL2D3V2 flapping mechanism.

2.2.3 The Geared Flapping Mechanism

The geared flapping mechanism (Figure 2-4) was different than prior iterations because it did away with the reciprocator altogether. This was desirable because the reciprocator needed to be sufficiently loose to allow any motion at all to occur, due to the increased tolerances necessary with a linear bearing. The geared flapper instead connected the output of the motor to a nylon gear, which was aligned with the flapping gears with a 1:1 ratio. The gears were connected to the flapping cranks, which were both attached to separate push rods, which in turn moved the wing mounts about their respective pivot points. This flapping mechanism had a nominal flap angle of $\pm 32^\circ$, but was adjustable by changing the attachment point of the push rods on the flapping cranks.

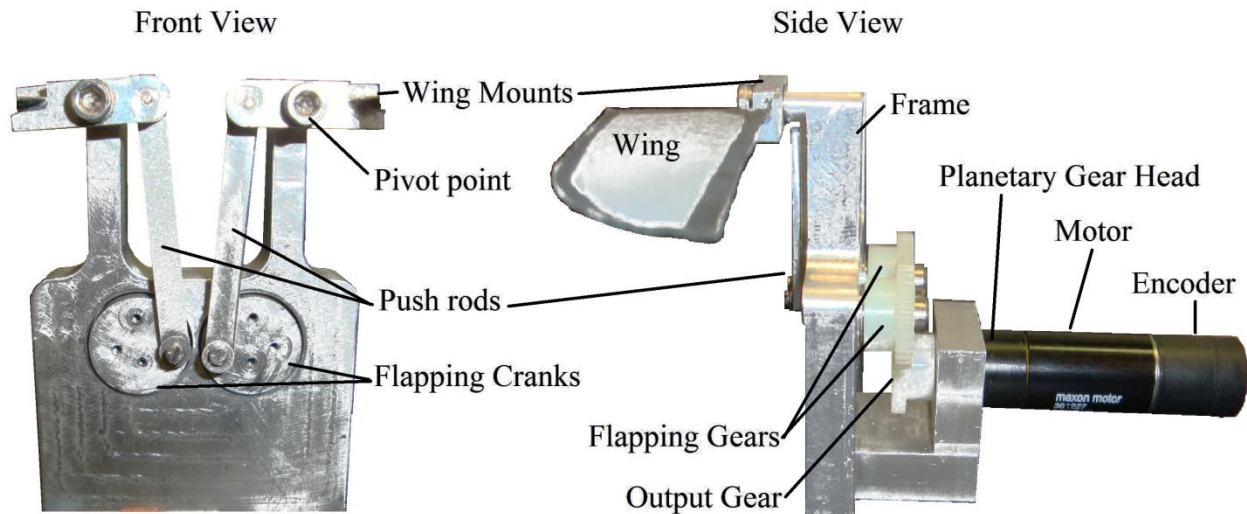


Figure 2-4. The geared flapping mechanism. Capable of 45Hz $\pm 54^\circ$.

This flapper, although larger and bulkier, had less parts than the previous versions, and due to the nature of the kinematics, had a much smoother sinusoidal flapping motion. Also, because of the absence of a linear bearing, the connections were allowed to be further tightened and slop was reduced. Not only this, but most of

the wear that would normally increase slop further, was mainly localized to the gears themselves, which are easy to inspect and replace.

2.3 Force Sensor

A 6-axis force sensor (ATI Industrial Automation's Nano17, <http://www.ati-ia.com/>), was used to measure the thrust and lift output of a given pair of wings. This sensor measures force with silicone strain gages, has a resolution of 0.318 grams-force, and its measured values were read into a computer system using a data acquisition device (National Instruments NI USB 6521, <http://www.ni.com/>). Flapping trials at various frequencies were performed for times ranging from 6-10 seconds. Tare measurements were first taken with the motionless flapper attached, and then the flapper was allowed to ramp up acceleration. Once the desired flapping frequency was obtained, samples were taken 500 times every flap cycle, and the entire data set minus the tare measurement was then averaged to find the average thrust and lift over the entire test duration.

Due to the fact that it was a single degree of freedom flapper, and that net lift should be zero, any lift component was assumed to be due to asymmetry in wing or flapper construction, and was usually much less than thrust force values. A wing's performance was therefore evaluated based on thrust production alone. Also, the Flapping mechanism was mounted on its side atop the sensor, so that gravity was neglected from any measurements. The full setup can be seen in Figure 2-5.

2.4 Digital Image Correlation

A common non-contact method of measuring the 3-dimensional deformation, known as Digital Image Correlation, was used to measure the kinematics of the wings as they went through the flap cycle. With DIC, the complex deformation shapes that the

wing experiences due to aerodynamic and inertial loading are obtained and used later for further analysis.

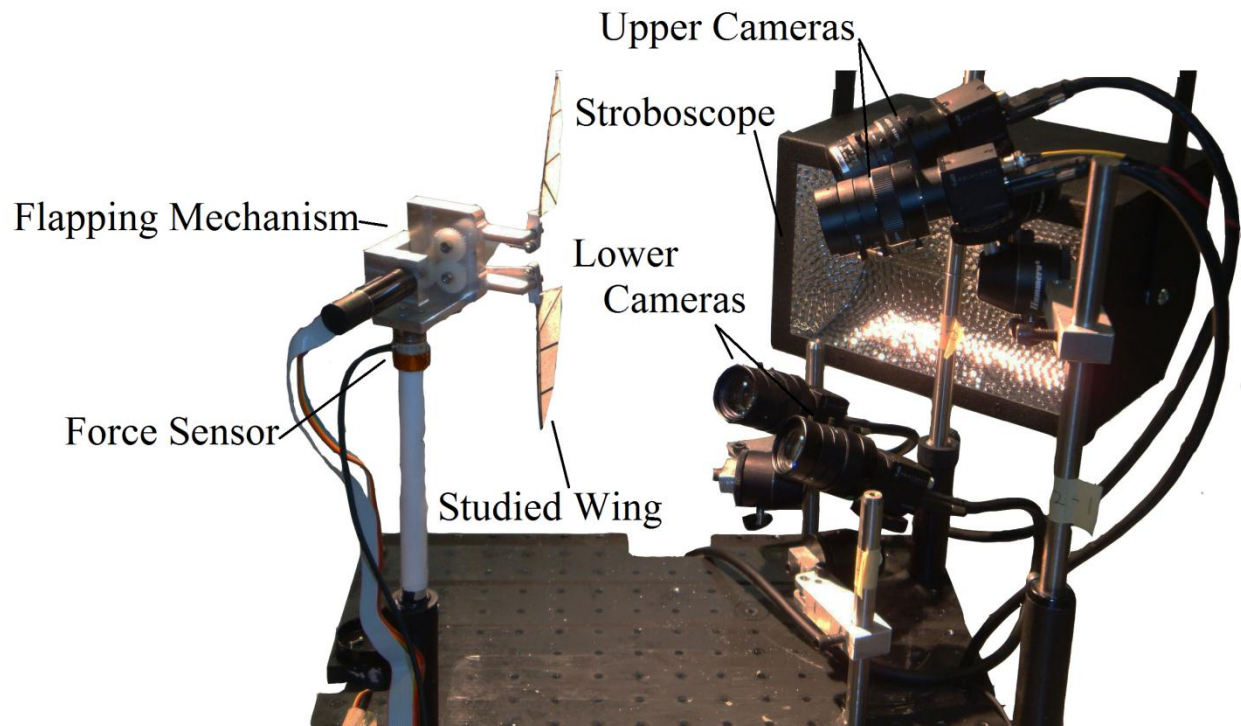


Figure 2-5. The experimental setup. The flapping mechanism is mounted sideways atop the force sensor for force measurement, while the two sets of stereo cameras capture the studied wing's deformation.

2.4.1 Camera and Lens Selection

The DIC system was comprised of 4 Point Grey Research Flea2 cameras divided into two sets. One set was arranged so that it captured the lower half of the flap cycle, while the other pair captured the upper half, and each pair captured a single studied wing in stereo-vision. The cameras were rigidly mounted so that relative motion between them was eliminated. Their resolution was 1624X1224, so that a fine speckle pattern could be applied to the wing, to allow for more accurate DIC. The overall size of these cameras was 29mm x 29mm x 30mm so that they could be placed in close proximity to one another as well as the flapping mechanism, and their large 1/1.8 CCD's

gave them high sensitivity. Also, the cameras high speed 1934-b 800 Mb/s digital interface was capable of transferring images at a frame rate of 15 FPS, while all four cameras took pictures almost simultaneously via an external trigger, with a maximum deviation of 125 μ s.

The lenses used were Computar's 12-36mm F2.8 C-mount lenses. They were selected for their short focal length, and therefore wide angle of view. With these characteristics, a relatively large depth of field was achievable, which was necessary because of the large displacements the wings exhibited during flapping. For DIC to work correctly, in each image, each speckle must be in focus so that it may be correlated to a reference image. A large depth of field allows for this throughout the flap cycle. The lenses were zoomed in, and focused on a single wing, so that it took up a majority of the field of view.

2.4.2 Experimental Setup

The full layout of the experimental setup can be seen in Figure 2-5. A given pair of wings was attached to the flapping mechanism, and the entire mechanism was mounted sideways atop the force sensor (so that gravity was neglected). The flapping mechanism was actuated to flap at a single frequency, ranging from 10Hz to 40 Hz, and two channels of the force sensor were sampled to return average values of both lift and thrust for each tested frequency (Section 2.3).

Deformation data of the wing was also collected, via the DIC system. All 4 cameras in the system were zoomed in, and focused on the lower of the two wings on the flapping mechanism. The lower two cameras were arranged to capture the deformation from mid-plane to the lower extreme of the flap cycle, while the two upper cameras were arranged to capture the deformation from mid-plane to the upper

extreme. This made sure that at least one stereo image was taken for all possible flap angles of the flap cycle.

A random speckle pattern was applied to the surface of the wing, using a black spray paint, so that the DIC system could keep track of rigid body rotations and displacements. By making a random pattern on a surface, the DIC software could recognize unique parts of the flapping wing, and compare them to those same parts in the reference image. It is in this way that it could relate the un-deformed wing to its new position.

Due to the relatively long exposure time of the DIC cameras, compared to that of the fast acting flapping mechanism, blurring of the images with ambient light was an issue. This was solved with a stroboscope. A light pulse from the stroboscope was synchronized with the capture time of the 4 cameras, so that it would flash at the necessary moment to capture a crisp picture of the speckled wing.

2.4.3 DIC Procedure

The first step was to set up the position and view of each of the cameras. The flapping mechanism was placed where it would be during testing, and the cameras were zoomed in to the lower wing, so that it took up the majority of the viewing field. The wings were then put through the flapping motion, and it was confirmed that they would be in view no matter the flap angle. The relative angle between each stereo set would be optimum at 45° for the most accurate out of plane displacement, but due to the excessive deformation seen during flapping, and the fact that the wing's pattern must be entirely in view of each camera, the angle was decreased to about 20° . The lower cameras were then focused on the wing when it was halfway between mid-plane and the lower extreme, and the upper cameras were focused on the wing halfway between

mid-plane and the upper extreme. The aperture was then closed, enough so that the depth of field encompassed a large enough area to capture any possible wing position in focus, but not too large to where there wasn't a significant amount of brightness. Gains were then adjusted so that the image was clearly visible. The cameras were then rigidly locked in place and not adjusted.

Next a calibration grid was held in front of each stereo set of cameras. The calibration grid is a gridded series of dots held on a rigid plate, with a known spacing in between the dots. Three of these dots are unique, and are known as landmarks. The cameras collected calibration images of this grid in different positions, and estimated the position of the grid plane using these landmarks. The computer system then compared a modeled position of the rest of the dots, with their actual recorded position, and through an iterative process images were selected which decreased the standard deviation of this difference in distance.

Once the cameras were calibrated, the wing is placed at mid-plane, and a reference image is taken. This reference image is of the static un-deformed wing, and is used to compare every subsequent flapping image to. The way this comparison is done has to do with the unique speckle pattern applied to the wing. The computer system selects a certain subset search region, with a specific pixel distribution and intensity in the reference image. It then finds that same region in the deformed image taken during flapping, and can determine the new location and rotation in a three dimensional space. In this way a full field 3 dimensional wing displacement image of the deformed wing could be found. The flapping mechanism is then actuated, and

pictures were taken throughout the flap cycle. 3 dimensional structural wing deformations were recorded for the entire flap cycle.

2.4.4 Stroboscope and Trigger Timing

The main problem with the DIC system is that the cameras' frame rates are much lower than needed to accurately capture multiple points in the flapping motion. Even though maximum capture rate is 15 FPS for the cameras individually, when they are connected to the same bus, this drops precipitously to 5 FPS. To accurately capture the complex motions that occur up to 40Hz, a scheme is adopted to capture what is thought to be the next increment in the flap, in subsequent flapping cycles. This can be done with the major assumption that the flapping frequency is very steady, so that if the proper wait time is employed, sequential images can be taken from different cycles.

The trigger timing interval is determined with the following relationship:

$$\Delta T = \frac{N + \frac{1}{s}}{m}$$

Where ΔT is the trigger timing interval, N is the number of cycles between each trigger, s is the number of samples per cycle, and m is the steady state flapping frequency. Knowing the trigger interval of the camera, the stroboscope was set at a flash frequency f of:

$$f = \frac{1}{\Delta T} = \frac{ms}{Ns + 1}$$

This capture scheme works very well for extremely steady flapping, but at higher flapping frequencies the method tends to break down. With the higher loads attributed to the higher frequencies, the motor must make adjustments to the output torque to compensate for large force variations. In the process, the frequency tends to slightly

vary, and makes it so that each cycle may not be identical. Because of this, the images taken at higher flap frequencies must later be re-arranged later in post processing, based on the calculated flap angle so that sequential order is achieved, or images out of sequence were removed.

The stroboscope is used as the light source to illuminate the flapping wing, and is triggered by the shutter of the DIC cameras. It emits an 8-10 μ s pulse that allows the cameras to only capture a brief clear image of the wing, despite their long exposure time. An issue that arises due to this is that the wing is sometimes silhouetted, and the batten structure throws a shadow across parts of the speckled surface of the wing. For DIC to correctly work, it must always be able to identify the speckle pattern to achieve correlation, so methods to alleviate the mismatch between reference image and deformed image must be employed.

By enlarging the subset size, these discontinuities can sometimes be jumped over, but at the cost of reduction in spatial resolution. The main method used was to edit the deformed image in Adobe's Photoshop, and adjust the brightness and contrast in the area of the batten's shadow. In this way, the deformed image was corrected to allow the computer to accurately find the correct subset, and allow accurate matching to occur.

CHAPTER 3 ANALYSIS TECHNIQUES

3.1 Main Hypothesis

The first and foremost goal of this paper was to associate certain deformations of the dynamic motion of the wing with the thrust output of that wing. The main hypothesis being proposed is that bending along the chord (c) of the wing, or what will be referred to in the rest of the paper as 'twist about the leading edge', improves thrust output. If this hypothesis is correct, the structure of a particular wing can be made to be compliant in torsion about the leading edge, and can therefore produce more thrust.

This idea is not novel, because it is known that in a single degree of freedom flapper, such as the ones used in this paper, structural deformation is necessary to produce any net force.¹⁶ This is graphically illustrated in Figure 3-1.

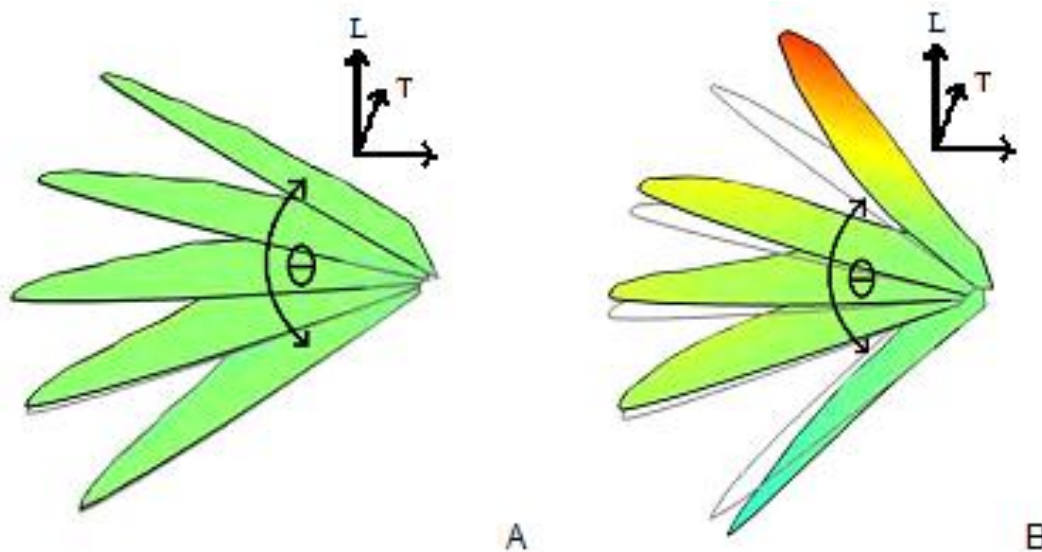


Figure 3-1. Visual comparison of wing rotating through a single degree of freedom flap angle θ . Lift L , is vertical, and thrust T is into the page. A) Structurally rigid wing, where no deformation occurs. B) Wing with a flexible structure, so that it is able to passively deform as it flaps.

In Figure 3-1A above, the wing experiences no deformation. Because it is restricted to the single degree of freedom , it pushes the same amount of air up in the upstroke, that it pushes down in the down-stroke, resulting in zero net lift L . Also, due to the fact that its 90° to the thrust plane, it is essentially at 90° angle of attack, or in other words it produces zero net thrust T .

By allowing the wing to passively deform, as seen in Figure 3-1B, the wing is able to twist about its leading edge. Although it still produces zero net lift, the passive deformation allows the wing to change its angle of attack relative to the flapping motion. Because of this, the wing is able to produce net thrust T .

Obviously this example is extremely over simplified. First of all, the angle of twist is constantly varying throughout the highly dynamic flap cycle. Aerodynamic and inertial forces are sinusoidal in magnitude, and are phase shifted, which translates to very complex kinematic motion. Also, even though twisting about the leading edge is a necessity, to be able to quantify something that doesn't vary constantly across the span of the wing proved to be quite complex. Another issue is if the structure is too compliant in torsion, and the wing is allowed to deform too much, the angle of attack of the wing essentially goes to zero, and again there is no net thrust. It is because of this that one must not just merely try and maximize twist, but optimize it for a given wing structure.

3.2 Post Processing of DIC Data

The data obtained from the DIC system, was processed into 3-dimensional images using Vic-3D software, then exported in ASC-II format, for further processing using Matlab. The 3-dimensional image of the wing needed to be rotated and translated from a local coordinate system, to a global one. To do this a series of steps was followed:
Step 1: the wing's angle in the X-Y plane was adjusted so that the chord ran along the

global X direction, and the span ran along the global Y direction. This was done visually because the wing's irregular shape and hand-made construction sometimes led to slight variations in final layout. Step 2: The wing image was then translated so that the corner of the rigid triangle resided at the origin of the global coordinate system. These first two steps are illustrated in Figure 3-2A and Figure 3-2B respectively.

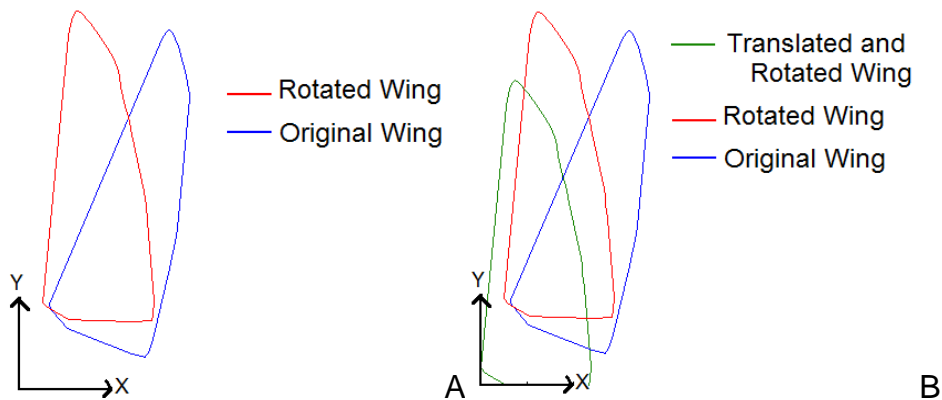


Figure 3-2. How the wing is rotated and translated. A) Step 1: The original wing was rotated so that its span ran along the Y axis, and its root ran along the X axis. B) Step 2: The wing was translated so that its corner resided at the origin of the coordinate system.

Then the final rotation was taken care of in step 3. Step 3: The wing's orientation was further adjusted so that if the wing were un-deformed, it would lie flat in the X-Y plane. This was done by finding 3 points in the plane of the rigid triangle, which was assumed to be un-deformed. Because the wing was already rotated in the X-Y plane, it was simple to choose 3 point locations that were arranged so that 2 are parallel with the X and Y axes. Using the unit vectors between these points (whose locations were interpolated onto the surface of the rigid triangle), and their cross product which is normal to the plane, a coordinate transformation was found to rotate the wing so that its un-deformed plane resided in the X-Y plane, as seen in Figure 3-3.

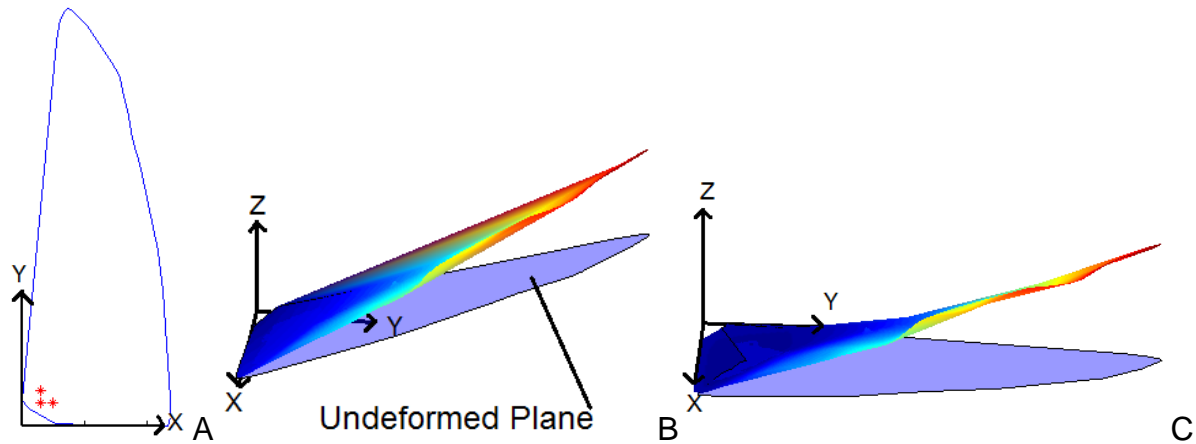


Figure 3-3. How the wing is further transformed. A) The red dots shown reside on the un-deformed rigid triangle. B) Once the unit vectors are found, an un-deformed plane for the wing is created. C) Step 3: The wing is oriented so that its un-deformed plane resides in the X-Y plane.

This final orientation made it so only deformation would be out-of-plane, which eliminates angle change due to flap angle, and makes comparison much simpler. Flap angle is still recorded, but only in numerical form. This orientation is also desirable because it is similar to the output orientation used in finite element software, which is used later in this paper as a model for wing deformation. Direct comparison between the DIC data and the finite element model is therefore possible with minimal effort.

3.3 Selected Variables for Analysis

3.3.1 Twist at Span-wise Locations

As was stated earlier, the major assumption was that increased twist can be related to increased thrust, but twist along the wing can be very difficult to depict. The first method used was to choose different locations along the span, and find the angle of twist along that line. The minimum and maximum z-coordinates were found on lines that were at 25%, 50%, and 75% of the span, and the angle between them was considered to be the twist along that line. This method was far from perfect, because it

neglected variations in twist due to bending along the leading edge, and the fact that it was 3 separate variables to relate twist to. It was found to be difficult to characterize twist with a single variable because it did not vary constantly along the span for a given wing. This first method of analysis is shown in Figure 3-4.

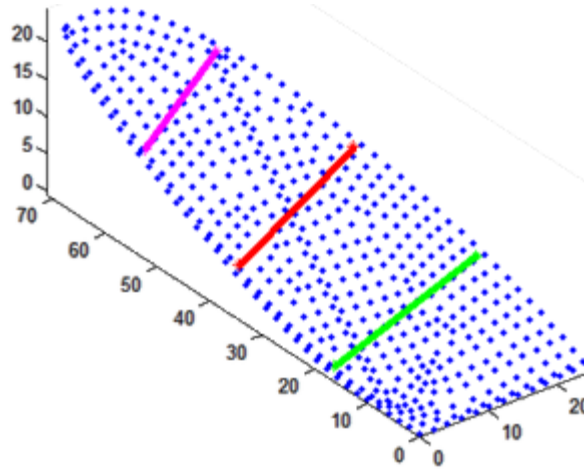


Figure 3-4. Twist is measured at different percentages of the total span, at each of the lines shown. The green line is α_{25} , the red line is α_{50} , and the magenta line is α_{75} .

3.3.2 Enclosed Volume and its Centroid

A more convenient way to characterize the behavior of a particular wing's deformation throughout the flapping cycle is to calculate the volume enclosed by this wing's deformation and the centroid of that volume. A simple way of describing this enclosed volume is the volume between the deformed wing and its "shadow" (Figure 3-5). The volume itself is a single value that is a quantitative measure of the overall deformation, but the centroid of this volume gives the researcher more pertinent information. Specifically, the span-wise location of the centroid of this volume can be related to the amount and distribution of bending in the wing, while the chord-wise location of the centroid can be related to the overall twist. With these measurements, a large amount of data can be whittled down into a few key variables.

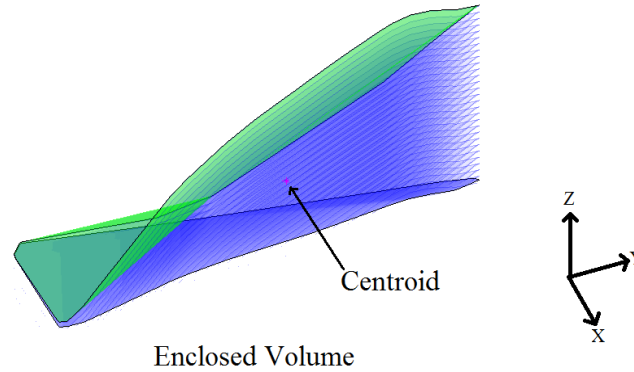


Figure 3-5. A depiction of the enclosed volume under the wing, and its centroid.

To calculate the volume an integration technique was used. In Matlab, the entire wing in the X-Y plane was broken down into a series of smaller boxes, and the surface of these boxes was integrated using the quad2d function. The quad2d function interpolates between the data points of the wing, and uses these smaller boxes as bounds for the integration. The volumes of these individual boxes are then summed to comprise the total volume.

To find the centroid of the enclosed volume, the center of each small box is considered the centroid of that box (which is a good assumption if the boxes are significantly small). Using knowledge on the definition of a centroid,¹⁷ the x location of the centroid is:

$$X_c = \frac{\int_A x \, dA}{A} = \frac{\sum_i x A_i}{A} \quad \text{and similarly for the y location: } Y_c = \frac{\int_A y \, dA}{A} = \frac{\sum_i y A_i}{A}.$$

X_c and Y_c are the X and Y centroid locations respectively, x is the distance x from the origin to the center of a particular box, y is the distance y from the origin to the center of the box, and A_i is the area of each box. By summing the weighted centroids of each of these individual boxes, the centroid location of the entire wing is found.

Obviously the size of the box has a major influence on the quality of the result due to the fact that an irregularly shaped wing is being divided into square subsections. As can be seen in Figure 3-6 the smaller the box, the better coverage it has of the entire wing, and therefore the more accurate the result. Minimizing box size is one factor in deciding desired box size.

It can be seen in Figure 3-6 that the coarse mesh leaves out large sections of the wing, and therefore has a less accurate answer. The accuracy of the coarser mesh is further compromised because the sections of wing that it leaves out of its calculation are the parts that undergo the largest deformations. This can also be seen in Figure 3-7, where there seems to be an approximately linear relationship between reducing box size and the calculation of volume, as well as the x and y coordinate of the centroid. As the box size is reduced, the calculations for these variables converge to the most accurate answer. The problem is that by minimizing the box, the run time of the program makes using this method undesirable. So the second factor in deciding box size is time.

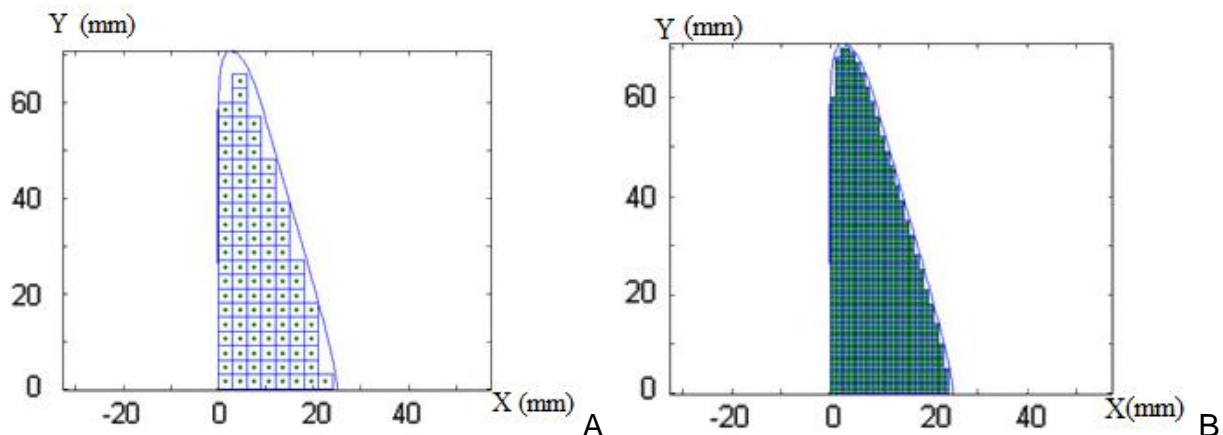


Figure 3-6. Wing divided into boxes outlined in blue, and their centroid is shown with a green dot. A) A wing divided into boxes measuring 3mm X 3mm. B) The same wing divided into boxes measuring 1mm X 1mm.

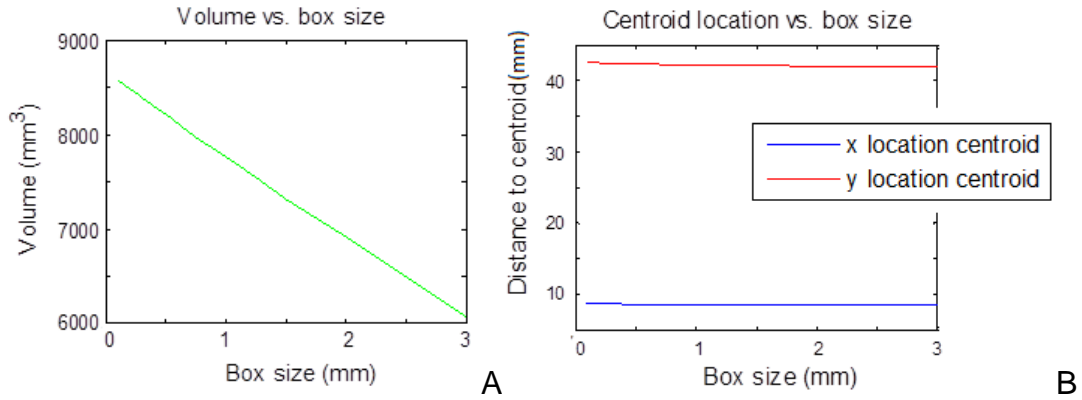


Figure 3-7. Volume and centroid vs. box size. A) Graph of calculated volume vs. box size. B) Graph of calculated X and Y centroid location compared to box size.

It can be seen in Figure 3-8 that when the box size becomes too small there is an obvious time issue. The benefit of having a more accurate volume and centroid calculation does not outweigh the massive time cost associated with minimizing box size. For a box of dimensions 0.1mm by 0.1 mm, the simulation takes over 40 minutes for one wing image.

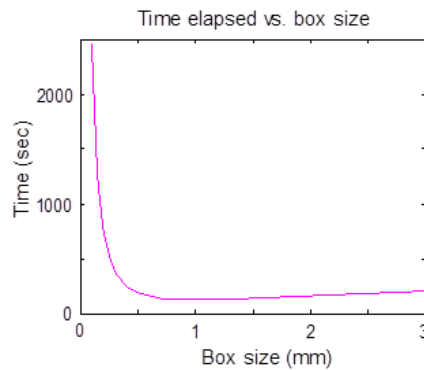


Figure 3-8. Graph of chosen box size vs. elapsed time to calculate enclosed volume.

Instead of settling for a coarse box division due to time constraints, I instead adjusted the code to minimize calculation time. Rather than using the costly quad2d function to integrate over the box, the 4 corners of each box were averaged and assumed to be the height of each box. This method drastically reduces calculation time, and converges with the integrated answer as box size is decreased (Figure 3-9).

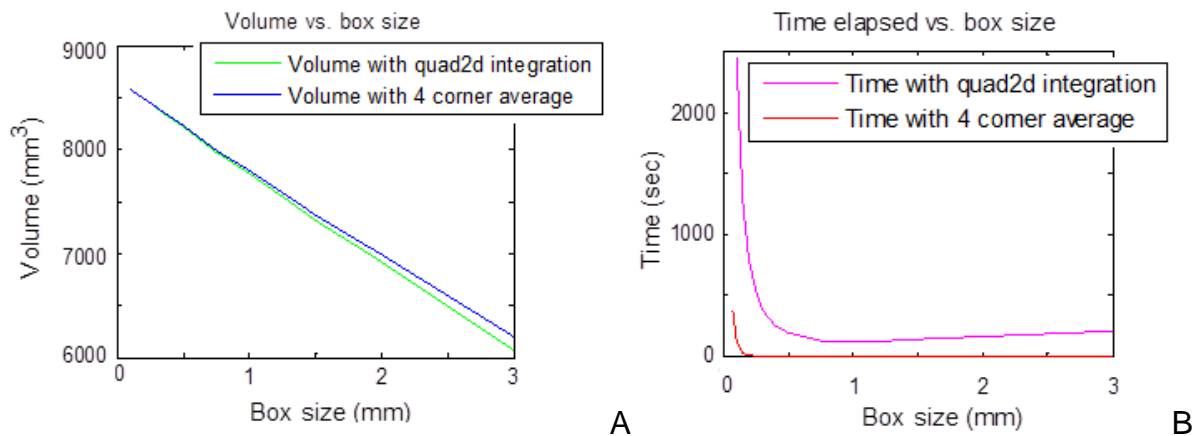


Figure 3-9. Comparison graphs between quad2d integration and 4 corner average techniques. A) Box size vs. enclosed volume comparison. It can be seen that the two answers converge. B) Box size vs. elapsed time to calculate volume.

This 4 corner averaging method is far faster than the interpolating method, and the answers for the calculated enclosed volumes do converge to a common number (as they should as the smaller boxes fill the curved areas better). The problem is the centroid location seems to diverge as the boxes get smaller than about 1mm (Figure 3-10). The reason for this divergence is that some areas of the surface of the wing near the trailing edge extremities are concave.

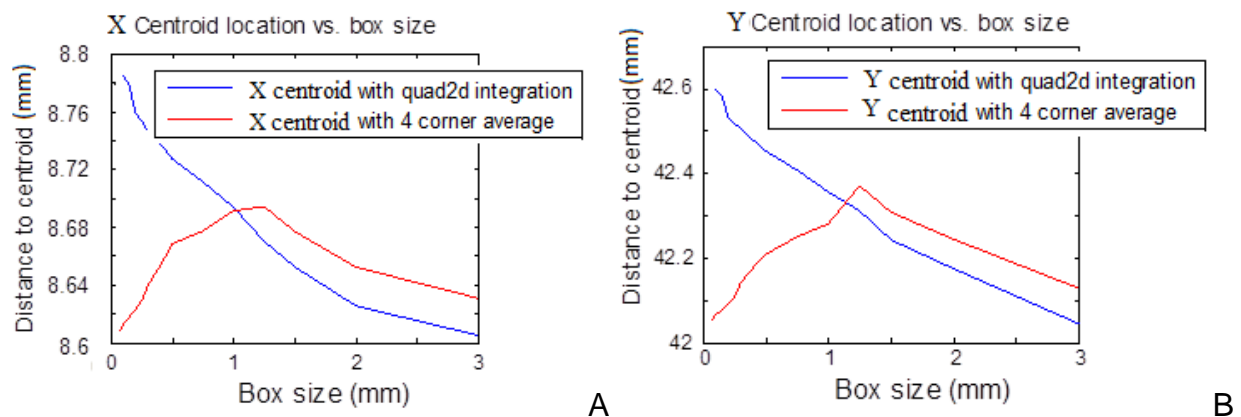


Figure 3-10. Comparison graphs between quad2d integration and 4 corner average techniques. A) Box size vs. X centroid location comparison. B) Box size vs. Y centroid location comparison.

Because of this concavity, the averaging method underestimates the volume at these points, and therefore skews the centroid location towards the corner of the root and leading edge (bottom left corner). This weighting effect is minute, and it doesn't present itself until the mesh is sufficiently small, but Figure 3-11 is inserted to prove why there was a divergence in centroid location. Blue dots represent areas where the averaging method calculates a lower volume than the integration method:

Underestimation of Calculated Volume using the Averaging Method

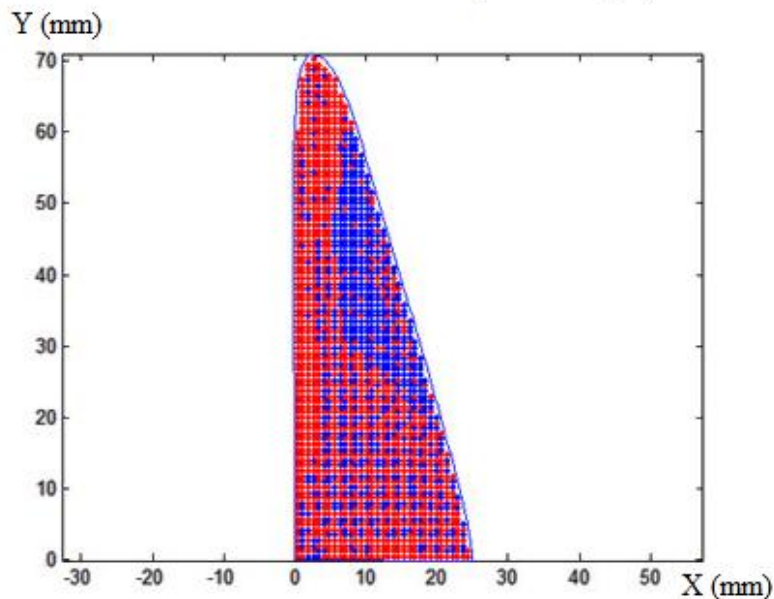


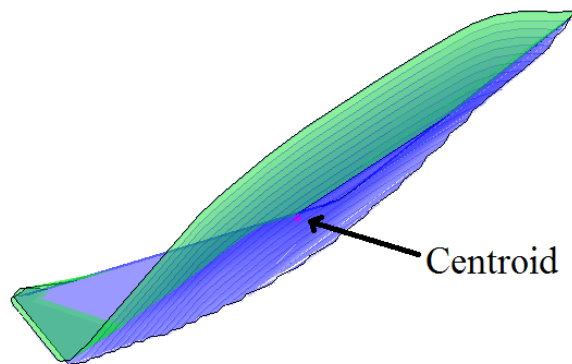
Figure 3-11. A visual reason for the divergence of the X centroid using the averaging method. This graph has a box size of .75mm X .75mm. The concentration of the under-estimation of the volume can be seen at the mostly concave trailing edge of the wing.

Because the reason for the divergence was found, and there is confidence in the faster method, the averaging method was used as the method to find enclosed volume and centroid location. Box size of 1mm X 1mm is used because it is fast and robust enough to calculate the correct value of the centroid.

3.3.3 Twist Volume and its Centroid

The previous method of calculating volume was very robust, and had the ability to capture complex deformations in a minimal amount of variables, but it had a drawback, specifically in regards to accurately depicting twist. It was seen that a given enclosed volume's centroid was heavily influenced by the presence of a large amount of bending along the leading edge. This was because large amounts of bending caused high tip deflections, and the centroid was essentially weighted to move towards the wing tip. This was undesirable, because a wing which experienced large amounts of bending returned centroid locations which did not mirror its twist.

A simple method was employed to correct this. In the previous enclosed volume method, the height of each box was taken from the average Z height of that box to $Z=0$. In the twist volume method, the lower bound for the height of each box was a surface that followed the contour of the leading edge. This is graphically shown in Figure 3-12.



Twist Enclosed Volume

Figure 3-12. Figure depicting the twist enclosed volume, and its centroid. It can be seen that the lower surface of the volume follows the contour of the leading edge.

By selecting the lower bound for the twist volume calculation in this way, contributions that skew the centroid towards the wing tip are eliminated, and this volume essentially captures only the volume due to twisting about the leading edge.

3.4 DIC Data Analyzed Using the Selected Variables

To determine if the selected variables were indeed indicative of what they claimed to be, a series of post DIC analyses were completed on 3 preliminary wings. The chosen wings' layouts are shown in Figure 3-13. The wings were all chosen for specific reasons. The Hum wing's radial battens were inspired by the biological example of a hummingbird's wing. The LEO wing was the simplest of the 3, as its structure contained only a leading edge and a root batten. This translated to a lighter structure, which was the most flexible due to lack of support. The final wing was the PR or perimeter reinforced wing. This wing was similar to the LEO wing, but also had a supported trailing edge, which allowed for added inertial loading on the reversal in the flap stroke. Each of these wings' deformation images were collected for their entire flap cycles using DIC, and multiple tests at frequencies ranging from 15Hz to 30Hz were performed on them.

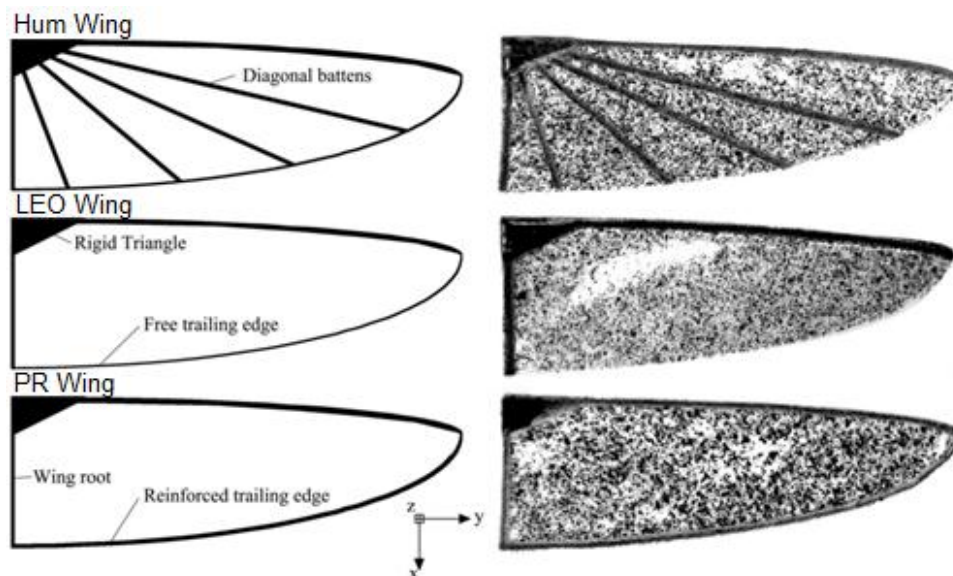


Figure 3-13. The three preliminary wings chosen for the post DIC analysis are shown above. Each wing has its ideal layout on the left, while a picture of the final constructed and tested wing is on the right. Courtesy of Pin Wu.

The main purpose of using the selected variables to analyze these wings was to relate specific variables that describe wing deformation to thrust output of the wing. This was done in tandem with the creation of a finite element model of a wing, in the hopes of creating untested wing structures in the model, and being able to determine if these structures would be viable candidates to produce more thrust if built. For reasons explained later in this paper, the model only represented a single flap angle in the flap cycle, that at mid-plane or zero degrees. It was because of this, that the analysis of the 3 preliminary wings was solely based on flap angles lying between -5° and $+5^\circ$.

The selected variables were graphed vs. output thrust for each wing, at each tested frequency. It was seen that the twist centroid's movement was highly correlated to thrust output of the wing, specifically the movement of the X and the Z centroid. Due to the fact that multiple values were plotted (all between -5° and $+5^\circ$), the range of values were shown as horizontal error bars, and their mean denoted as a symbol. The X centroid vs. thrust is in Figure 3-14, and the Z centroid vs. thrust is in Figure 3-15.

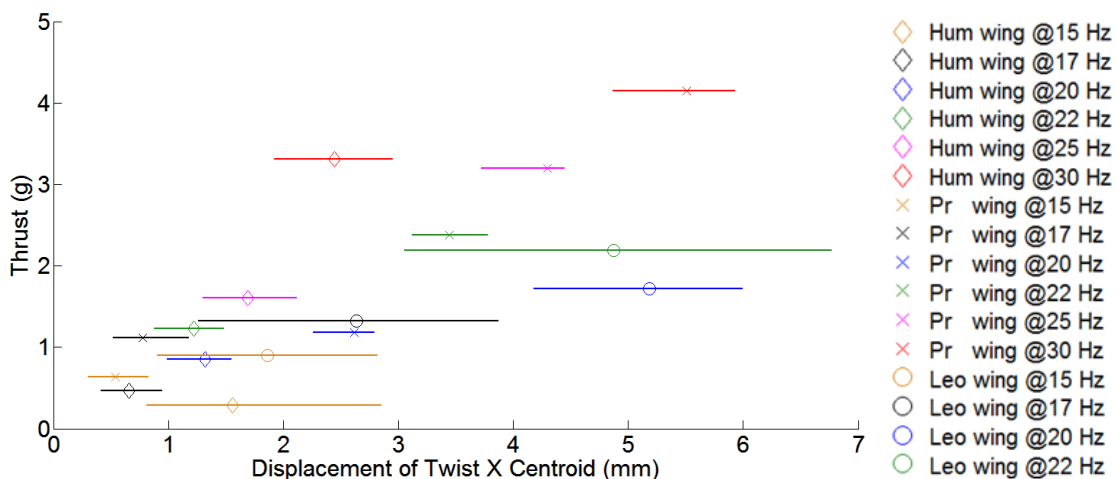


Figure 3-14. The displacement of the X centroid vs. thrust. Every frequency is in the same color, and a general positive correlation between X centroid movement, and increase in thrust can be seen. The error bars represent the range of values between flap angles of -5° and $+5^\circ$, and the symbol for that wing lies on the mean.

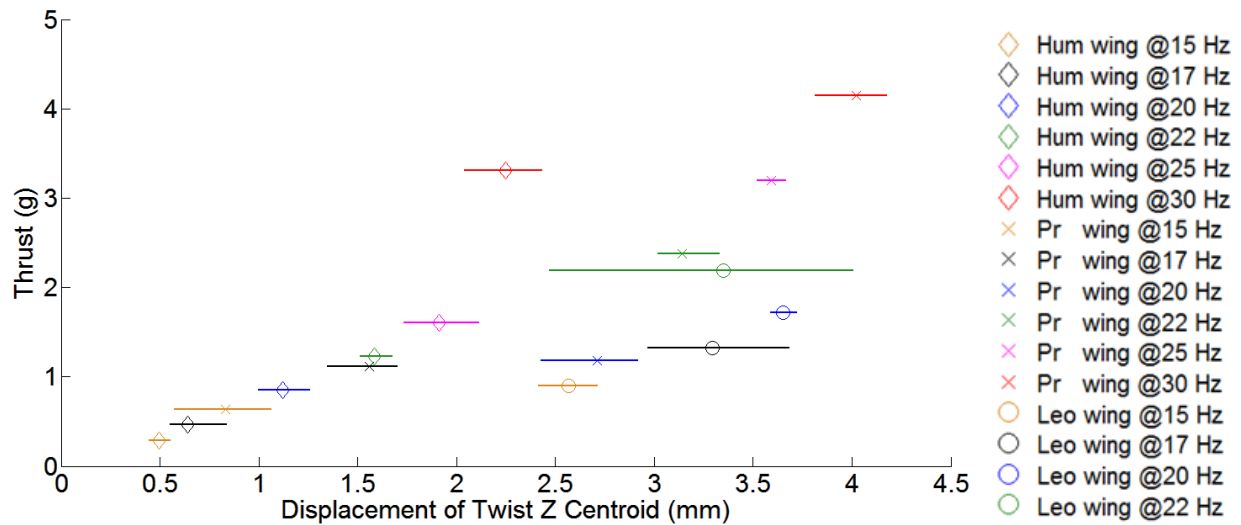


Figure 3-15. The displacement of the Z centroid vs. thrust. Every frequency is in the same color, and a general positive correlation between Z centroid movement, and increase in thrust can be seen. The error bars represent the range of values between flap angles of -5° and $+5^{\circ}$, and the symbol for that wing lies on the mean.

Some things about the above graphs need to be noted. First off, the LEO wing was only tested until 22 Hz because past this frequency, the wing would experience too much deformation and not produce significant amounts of thrust. Also, the displacement of the twist X centroid was in the negative X direction, or in other words increasing thrust would be related to the twist X centroid moving further inboard.

It can be clearly seen that, at a particular frequency, there is a general trend with the twist X centroid movement and thrust, as well as twist Z centroid movement and thrust. This movement of the centroid is actually truly related to the twist, as can be seen in Figure 3-16. As twist about the leading edge increases, the trailing edge sweeps in an arc in the positive Z direction, and the negative X direction. The twist X and Z centroids mirror this movement.

This correlation is not perfect, as can be seen in Figure 3-14 for 15Hz and 22Hz, as well as Figure 3-15 for 22Hz. Also, there are only 3 wings tested, and one of those

wings doesn't even work at higher frequencies. All in all, the shortcomings of these correlations are realized, but considering the complexities of deformations, and the fact that only one idealized flap angle is being considered, this simplified correlation is still deemed relevant. Of course, another plus is the fact that it gives clout to the main hypothesis, that increased twist is related to increased thrust.

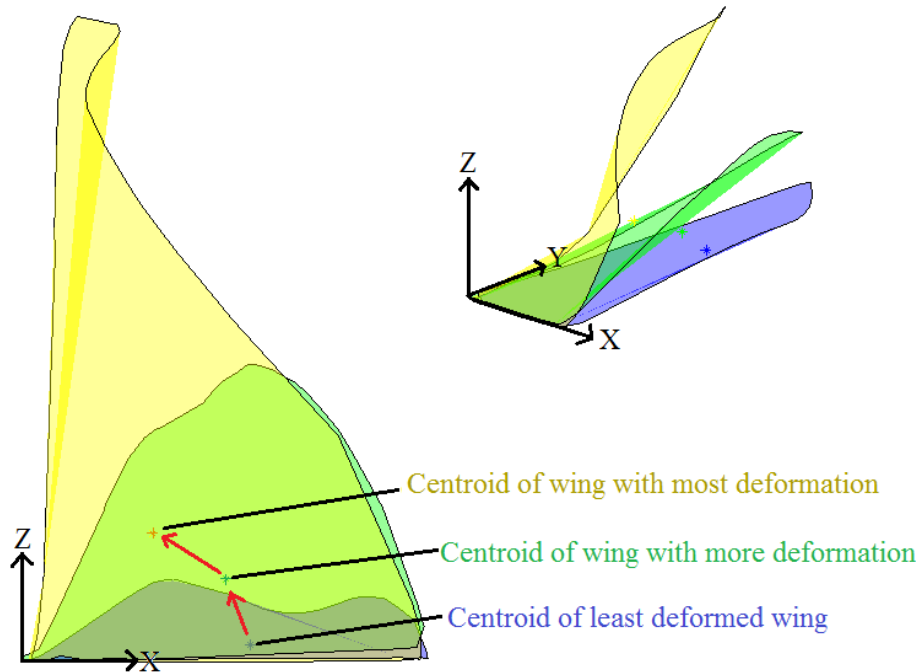


Figure 3-16. The movement of the centroid in the X-Z plane as twisting deformation increases. The least deformed wing, the blue wing, has a centroid location in the positive X direction, and is close to the Z axis. As deformation increases, the centroid moves in the negative X direction and positive Z direction.

There is also another trend that was noted when analyzing the 3 preliminary wings. As was stated before, the LEO wing's performance broke down at higher frequencies. The reason for this was excessive deformation at those frequencies, where the wing was too flexible, which allowed the wing to twist too much and go to zero degrees angle of attack.⁹ A way to describe this using the selected variables is, if there is a sudden drop in enclosed volume as frequency increases then the wing could

be showing signs of excessive deformation and may not perform well with the attributed higher loads. This can be seen in the Leo wing in Figure 3-17.

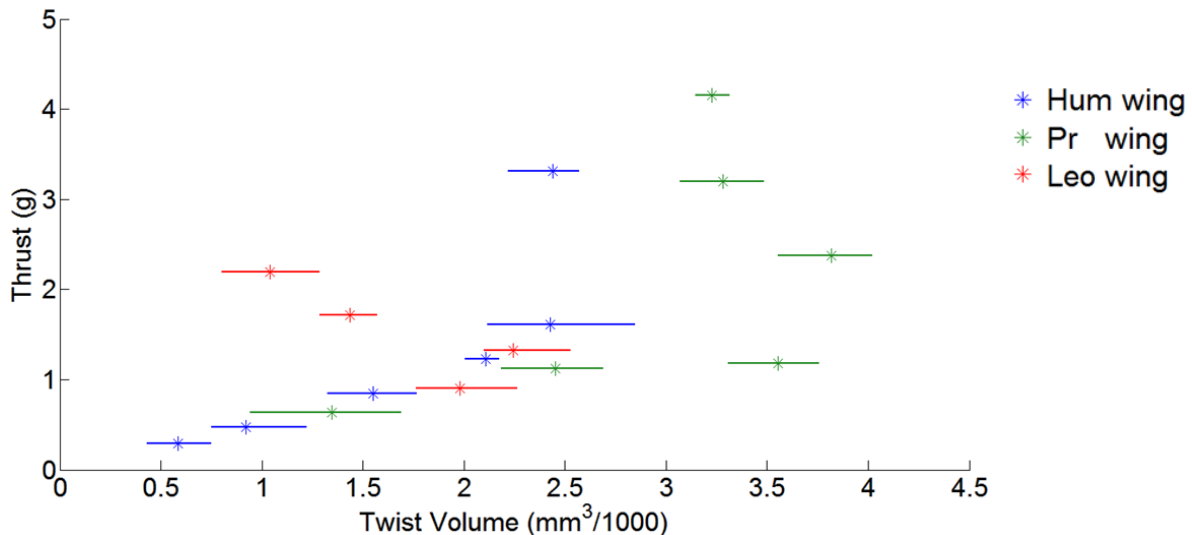


Figure 3-17. The change in enclosed twist volume vs. thrust. Every wing is shown in the same color, for all tested frequencies. The error bars represent the range of values at flap angles between -5° and $+5^\circ$, and the symbol for that wing lies on the mean. A sharp decrease in enclosed twist volume can be seen for the LEO wing right before it stops functioning correctly.

3.5 FE Model of the Wing

3.5.1 Justification for FE Model

The use of a finite element model was deemed appropriate because a tool was needed to come up with promising designs for wing construction. As is stated later in Section 3.7, it takes an extensive amount of time to physically construct and test a wing. Because of this, it was convenient to have a tool to guide wing construction, so that only those wings that show promise in a model are actually built.

3.5.2 Reason for the Selection of Mid-plane for the Model

The flapping cycle is very complex from a loading standpoint. A wing experiences different aerodynamic and inertial loads throughout the flap cycle, and is highly dynamic in nature. This complex loading was found to be difficult to model in Abaqus, a finite

element software. Instead of attempting to model the entire cycle, it was desirable to model a single point in the flap cycle, where the type of loading was well known.

Zero degrees flap angle, or mid-plane was selected for multiple reasons. The first being, that at this point in the cycle, it travels at the highest velocity as can be seen in Figure 3-18. Due to this, the thrust generation at mid-plane would be greatest according to the 'quasi-steady' theory of force production. This is also a point of zero acceleration. At this flap angle, the wing has just finished its acceleration, and is about to decelerate in preparation for the next reversal, and due to this lack of acceleration, inertial loading could be ignored. A single aerodynamic loading could be applied to the wing to accurately simulate what actually occurred at that point in the flapping cycle.

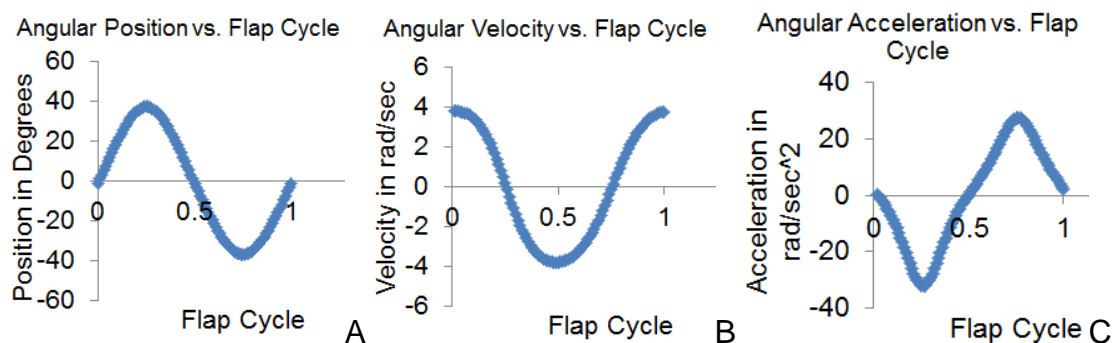


Figure 3-18. This is the angular position, velocity, and acceleration, at the wing mount of the current flapper. The flap cycle begins at mid-plane, and ends after one full cycle. It can be seen that acceleration is zero at mid-plane, and velocity is a maximum value.

3.5.3 Explicit vs. Implicit Analysis

The finite element program used, Abaqus, which offers two solvers. The first one is known as Abaqus Standard, which is an implicit solver that solves for true static equilibrium, and the second is Abaqus Explicit, an explicit solver that solves for dynamic equilibrium. In the early attempts at creating a model, the implicit solver was used. Due to material complexity and large deformations, this method had difficulty converging.

The convergence issues were specifically due to the difference in stiffness in the modeled carbon fiber vs. that of the Capran membrane. The carbon fiber's elastic modulus was almost two orders of magnitude greater than that of the Capran, and the thickness of the carbon fiber was about one order of magnitude greater than that of the Capran. Because of this difference in stiffness ($E \cdot I$), when loaded, the carbon fiber would deform only a small amount, while the modeled Capran would deform a great amount more. The Capran would then wrinkle in places (Figure 3-19), and the implicit solver would fail to converge.

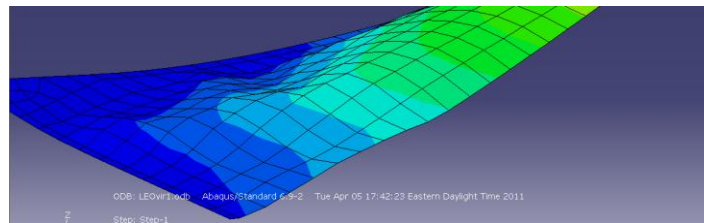


Figure 3-19. The wrinkling in the Capran membrane can be seen in this figure. Due to the irregular shaped elements, the implicit solver fails to converge

Because of these issues, Abaqus Explicit was chosen as the solver. This solver is more efficient at modeling 3-dimensional problems involving large deformations, such as those experienced by the wing. Using this solver, the model was able to converge.

3.5.4 FE Model Setup

Three wings were modeled in Abaqus that mirrored the three preliminary wings that DIC images were gathered for. Each of the wings created in Abaqus were of the same construction and the same nominal dimensions as the preliminary wings. Using the DIC images captured at zero degrees flap angle, for multiple test frequencies, the deformation between the preliminary wings and the modeled wings were matched.

Because the wing was very thin compared to its length and width, a 3-dimensional planar shell part was used. This part was subdivided using partitions, so that individual

section and material properties could be assigned, without the complexity of using multiple parts. There were 4 different section possibilities for each wing. 3 of them were carbon fiber of different thicknesses, mirroring the different amount of layers, and the final section was the Capran.

Table 3-1. List of sections used in the finite element model

Section name	Thickness	Material	Element type
CF 1 layer	0.19 mm	Carbon fiber	S4R- 4 node shell element
CF 2 layer	0.3 mm	Carbon fiber	S4R- 4 node shell element
CF 3 layer	0.4 mm	Carbon fiber	S4R- 4 node shell element
Capran	0.005 mm	Capran	M3D4R- 4 node membrane element

All of the section thicknesses described were accurate, except for that of the Capran. It was found that when modeled at the proper thickness of 14 microns, that the Capran would not deform properly. The modeled thickness of 5 microns was decided upon after multiple iterations were performed, and an amount of deformation that matched the DIC data was found. Shell elements were used for the carbon fiber due to their thin cross sections, while membrane elements were used for the Capran. Membrane elements have no bending stiffness, and based on the disparity in stiffness between the two materials, this was an accurate assumption for use on the Capran.

Material properties of the model were also chosen to match that of the actual materials. The carbon fiber had a density of 1966 Kg/m^3 , and was made as an elastic lamina. The individual properties were entered as follows: $E1 = 155\text{Gpa}$, $E2 = 12.1\text{Gpa}$, $\text{Nu}12 = .248$, $G12 = 4.4\text{Gpa}$, $G13 = 4.4\text{Gpa}$, $G23 = 3.2\text{Gpa}$.¹⁸ The Capran was made to have a density of 1160 Kg/m^3 , and was made as an isotropic material. It had a modulus of $E = 2\text{Gpa}$, which was slightly less than the actual modulus of Capran (2.5Gpa - 3.5Gpa), and a Poisson's Ratio of .3.

3.5.5 Load and Boundary Conditions

For each tested flapping frequency a linearly distributed load with a particular magnitude was applied to the modeled wing. The first method of choosing the appropriate magnitude for this distributed load was one of visual inspection, where a magnitude was iteratively chosen until the deformations between the modeled Abaqus wing and the DIC images of the tested wing were considered to be approximately equivalent. A pressure load, analogous to the aerodynamic load experienced at mid-plane, was applied to the model of the wing, which increased linearly with Y , from the root chord of the wing to the tip of the wing, as seen in Figure 3-20.

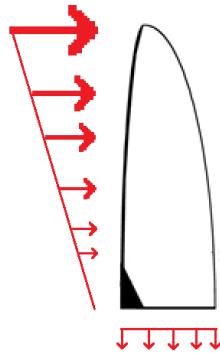


Figure 3-20. This is the distribution of the applied aerodynamic loading, used in Abaqus. It is a uniform distribution along the chord of the wing, which linearly increases as it goes towards the wing tip.

Because the explicit solver was used, the load had to be gradually applied. By default, Abaqus Explicit instantaneously applies loads, which could have induced a stress-wave which could propagate causing undesired results. By gradually ramping up the amplitude of the load using a smooth step, adverse effects were bypassed. The boundary conditions chosen mirrored the initial assumption that the rigid triangle at the base of the wing experienced no deformation. The entire 6mm X 12mm triangle was held stationary using an encastre boundary condition.

3.5.6 Adjustment of the Magnitude of the Distributed Load

The first method of finding the correct magnitude of the load, by visual inspection, was considered inadequate and subjective. This was exchanged for a more comprehensive method of reducing overall error. Of course each of the modeled wings didn't match perfectly with the DIC images, there was some error. This was first quantified by the following formula:

$$e_{adjusted} = \sum_{i=1}^n (Z_{i,ab} - Z_{i,DIC})^2$$

Where $Z_{i,ab}$ is a Z coordinate of the Abaqus model and $Z_{i,DIC}$ is a Z coordinate of a DIC image. The approximate error is the sum of the squares of the difference of each of these two coordinates.

There is an alternative way to calculate the magnitude of the distributed load to minimize the average error between the three modeled wings and the three DIC wings. This is a mathematical reason to choose a given magnitude, which is much preferred to the subjective test described earlier. By inserting a weighting factor λ into the following formulas:

$$e_{Hum: adj} = \sum_{i=1}^n (\lambda Z_{i,ab,Hum} - Z_{i,DIC,Hum})^2$$
$$e_{Leo: adj} = \sum_{i=1}^n (\lambda Z_{i,ab,Leo} - Z_{i,DIC,Leo})^2$$
$$e_{Pr: adj} = \sum_{i=1}^n (\lambda Z_{i,ab,Pr} - Z_{i,DIC,Pr})^2$$

Where $e_{Hum: adj}$ is the adjusted error between the Abaqus model and DIC image of the Hum wing, $e_{Leo: adj}$ that of the Leo wing, and $e_{Pr: adj}$ that of the Pr wing. The sum of these three makes the next equation:

$$e_{total:adj} = \sum_{i=1}^n (\lambda Z_{i,ab,Hum} - Z_{i,DIC,Hum})^2 + \sum_{i=1}^n (\lambda Z_{i,ab,Leo} - Z_{i,DIC,Leo})^2 + \sum_{i=1}^n (\lambda Z_{i,ab,Pr} - Z_{i,DIC,Pr})^2$$

Where $e_{total:adj}$ is the adjusted total error, λ is the weighting factor for the magnitude of the force, and $Z_{i,ab}$ and $Z_{i,DIC}$ are the Z coordinates for the three preliminary wings: the Hum, Leo, and Pr wings. By taking the derivative of the adjusted total error with respect to λ , and setting it equal to zero, an optimum weighting factor which minimizes the total error can be found:

$$\frac{\delta e_{total,adj}}{\delta \lambda} = \sum_{i=1}^n 2Z_{i,ab,Hum}(\lambda Z_{i,ab,Hum} - Z_{i,DIC,Hum}) + \sum_{i=1}^n 2Z_{i,ab,Leo}(\lambda Z_{i,ab,Leo} - Z_{i,DIC,Leo}) + \sum_{i=1}^n 2Z_{i,ab,Pr}(\lambda Z_{i,ab,Pr} - Z_{i,DIC,Pr}) = 0$$

And then solving for λ :

$$\lambda_{optimal} = \frac{\sum_{i=1}^n (Z_{i,ab,Hum} Z_{i,DIC,Hum}) + \sum_{i=1}^n (Z_{i,ab,Leo} Z_{i,DIC,Leo}) + \sum_{i=1}^n (Z_{i,ab,Pr} Z_{i,DIC,Pr})}{\sum_{i=1}^n (Z_{i,ab,Hum})^2 + \sum_{i=1}^n (Z_{i,ab,Leo})^2 + \sum_{i=1}^n (Z_{i,ab,Pr})^2}$$

This $\lambda_{optimal}$ is the optimum weighting factor to multiply the magnitude by to achieve the least amount of error between the models and the images of the three wings. This method was used to obtain the “best fit” of the model to the current DIC data. Included in Figure 3-21 is a graph of what the $\lambda_{optimal}$ is actually finding. Also, in Table 3-2, the final λ values, the approximate standard deviation, and the final calculated magnitudes are listed. Visual comparisons of the modeled wings and DIC wings are available in the Chapter 4.

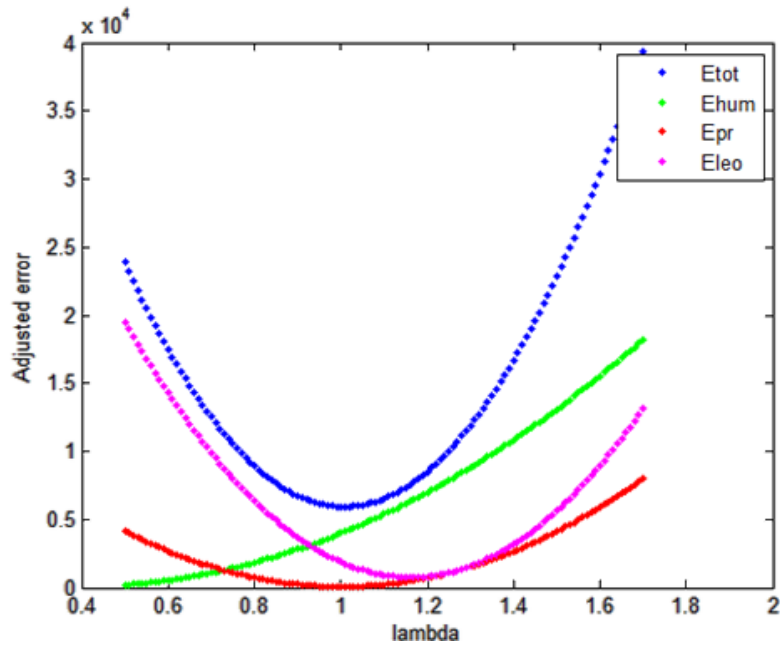


Figure 3-21. Graph of the adjusted error to a given lambda λ for the three wings at 15Hz. The errors of all of the wings are plotted with varying values of λ . The optimum lambda is the minimum of the total error plot Etot.

Table 3-2. List of the final λ used, the average error, and the magnitude of the load for each frequency. The adjusted error for each wing was divided by the total number of sample points, and then the square root was taken of this value. This more relevant error value e_{avg} could be thought of as the standard deviation. The last column is the finalized magnitudes of the distributed pressure load.

Frequency	Lambda	$e_{Hum: avg}$	$e_{Pr: avg}$	$e_{Leo: avg}$	Magnitude of load
15 Hz	1.007	4.11 mm	2.72 mm	3.49 mm	.165 Pa
17 Hz	.988	4.46 mm	3.88 mm	5.34 mm	.267 Pa
20 Hz	1.023	3.69 mm	2.89 mm	5.95 mm	.372 Pa
22 Hz	1.024	2.55 mm	1.37 mm	7.45 mm	.455 Pa
25 Hz	1.029	7.11 mm	5.67 mm		.801 Pa
30 Hz	1.011	4.99 mm	7.27 mm		.95 Pa

3.5.7 Advantage for the FE model

The reason that the finite element model is so advantageous is the low time cost compared to actually fabricating a wing and testing it. To actually build and test a single wing, one must: lay-up by hand the carbon fiber skeleton of a pair of wings (30

minutes). Cure the carbon fiber in an oven (7 hours). Speckle the Capran, adhere it to the wing, let this dry, then cut out the profile (20 minutes). Attach the wings to the flapping mechanism and test them at a range of frequencies (10 minutes). Then finally post process the information. Altogether, to measure the force a wing produces, this takes over 8 hours of time (does not include any digital image correlation). Now, multiple wings could be layed-up at once, so that the oven curing process could be done for multiple wings, but the time cost is still extremely high.

In stark contrast to this, the finite element model takes 15-25 minutes to run through all the frequencies for a completely new geometry. Although it isn't as good as physically testing a wing because it only simulates a certain flap angle, it is far more cost effective to weed out bad designs, and come up with good ones using the model. The model is therefore a very useful and powerful tool.

3.6 Candidates for Increased Thrust

To use the model, designs needed to be created that were thought to have the ability to increase thrust production. The deformations of the model were approximately equivalent to those of tested wings. Due to this, it was assumed that the selected variables of the modeled wing would give a good indication on whether these wings would generate high thrust if they were built. Novel designs were run through simulations in Abaqus, and the movement of the centroid of the twist enclosed volume was graphed. If the movement was significant, and there wasn't a sudden drop in enclosed volume (due to too much compliance), then the wing was thought to be an ideal candidate for increased thrust.

Different design strategies to increase torsional compliance were employed. One of these was changing the attachment point of the batten at the root of the wing. All

three of the preliminary wings had a batten stemming from the rigid triangle that ran along the root chord of the wing. The problem with this was the root of the wing was what experienced almost no forces at all (Figure 3-20). Due to this, deformation at the root was mostly caused by the Capran pulling the root batten, and this root batten was thought to limit deformation. In many of the tested designs, the attachment point at the root was changed.

Another approach was to reduce the bending stiffness of the battens by introducing jogs in their geometry, or changing the orientation they were in. Yet another idea was to change the leading edge. By adding another spar parallel to the first leading edge, but keeping one attachment point, the leading edge became stiffer in bending and less stiff in torsion. Ideas that looked into changing the cross section of the leading edge were also investigated. Many concepts were explored, in lots of combinations to try and elicit the desired behavior.

3.7 High Speed Camera Analysis

Although the DIC system could capture wing deformation with reasonable accuracy at lower frequencies, at high frequencies large variable forces would cause small variations in frequency. This would make it so the trigger timing of the DIC system did not allow for images to be taken sequentially (Section 2.4.4). Because of this, some behavior at high frequencies was sometimes hard to portray, especially when that behavior led to unsteady flapping (which the DIC system cannot show). A Vision Research Phantom V710 digital camera that was capable of capturing up to 1.4 million frames per second was used to give insight into some of the more complex behavior.

An issue was found with some of the iterations of the PR wing. At certain times an audible noise could be heard, and during this time flapping seemed to be very erratic.

The motions of the flapping wings were recorded with the high speed camera and analyzed. In attempts to reduce torsional stiffness, the root was disconnected from the rigid triangle and attached in different locations on the leading edge. By doing this, the once rigidly supported trailing edge was allowed to deform by large amounts compared to its stiffer leading edge counterpart, and its release of energy caused a shockwave to go through the wing. This undesired side effect was captured in the images shown in Figure 3-22.

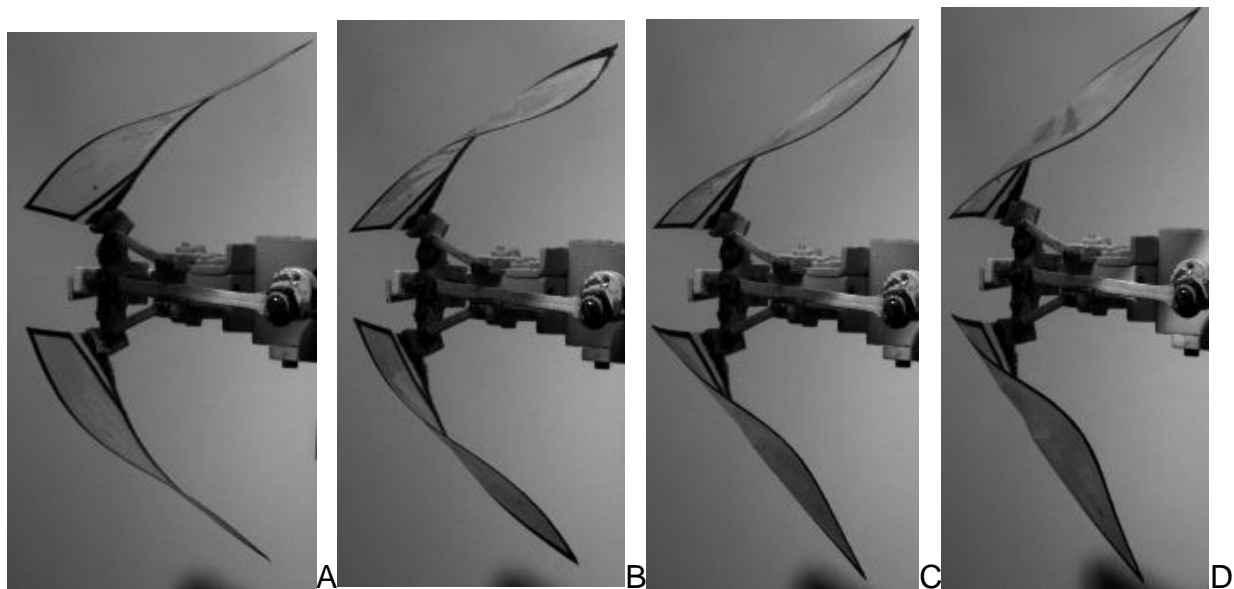


Figure 3-22. Image sequence of shockwave going through the trailing edge of a perimeter reinforced wing without rigid root attachment.

This phenomenon was evident in all of the wings with a supported trailing edge, but each one to different extremes. The amplitude of the shockwave was related to how rigid the attachment of the trailing edge was. For instance the preliminary wing, the PR wing, had a very minute shockwave, while that in Figure 3-22 was quite large. The kinetic energy caused by this event would either cause constructive or destructive interference, depending on exactly where the wing was in the flap cycle. It was hypothesized that this interference was the cause of the irregular flapping, and the

release of energy was the source of the noise. All in all, the high speed camera was able to capture the exact motion as it happened, and analysis using it was found to be worthwhile.

CHAPTER 4 RESULTS AND DISCUSSION

4.1 Visual Comparison of DIC Data and Model Output

The Abaqus model was numerically validated in Section 3.5.6, but it was considered useful to the reader if a visual comparison between the DIC wings at or near 0° and the wing modeled at 0° were shown (Figure 4-1). Certain choices in model parameters were made particularly to ensure matching between these two data sets. Specifically, the modeled thickness of the Capran needed to be significantly lower than the actual thickness of the Capran to allow the flexibility that actually occurs on the wing. It is evident by looking at the results from the Leo wing (which had no batten reinforcement, and therefore best exhibited Capran's behavior) in Figure 4-1E and Figure 4-1F, that accurate matching between the flexibility of the actual and modeled wing's Capran was achieved.

It can also be seen in Figure 4-1 that the varying complex behavior exhibited by each wing was simulated by the model with reasonable accuracy. The modeled Hum wing showed similar bend and twist behavior to the actual Hum wing. The modeled Pr wing showed the increased bending, and the smaller amount of twist that was evident in the graph of the actual Pr wing (this was due to the increased stiffness from the supported trailing edge). Also, the modeled Leo wing showed the increased amount of twist that was apparent in the increased deflection of the trailing edge.

Overall, the model was not an exact match to the DIC data images (Table 3-2), but it did a good job of simulating the behavior of each of the three wings. Considering that the objective of the model was only to find wing designs which showed promise of increased twist, the only necessity of the model was that it was able to simulate the

types of deformation that a wing experiences under loading. Based on the visual comparison, this accurate simulation is evident.

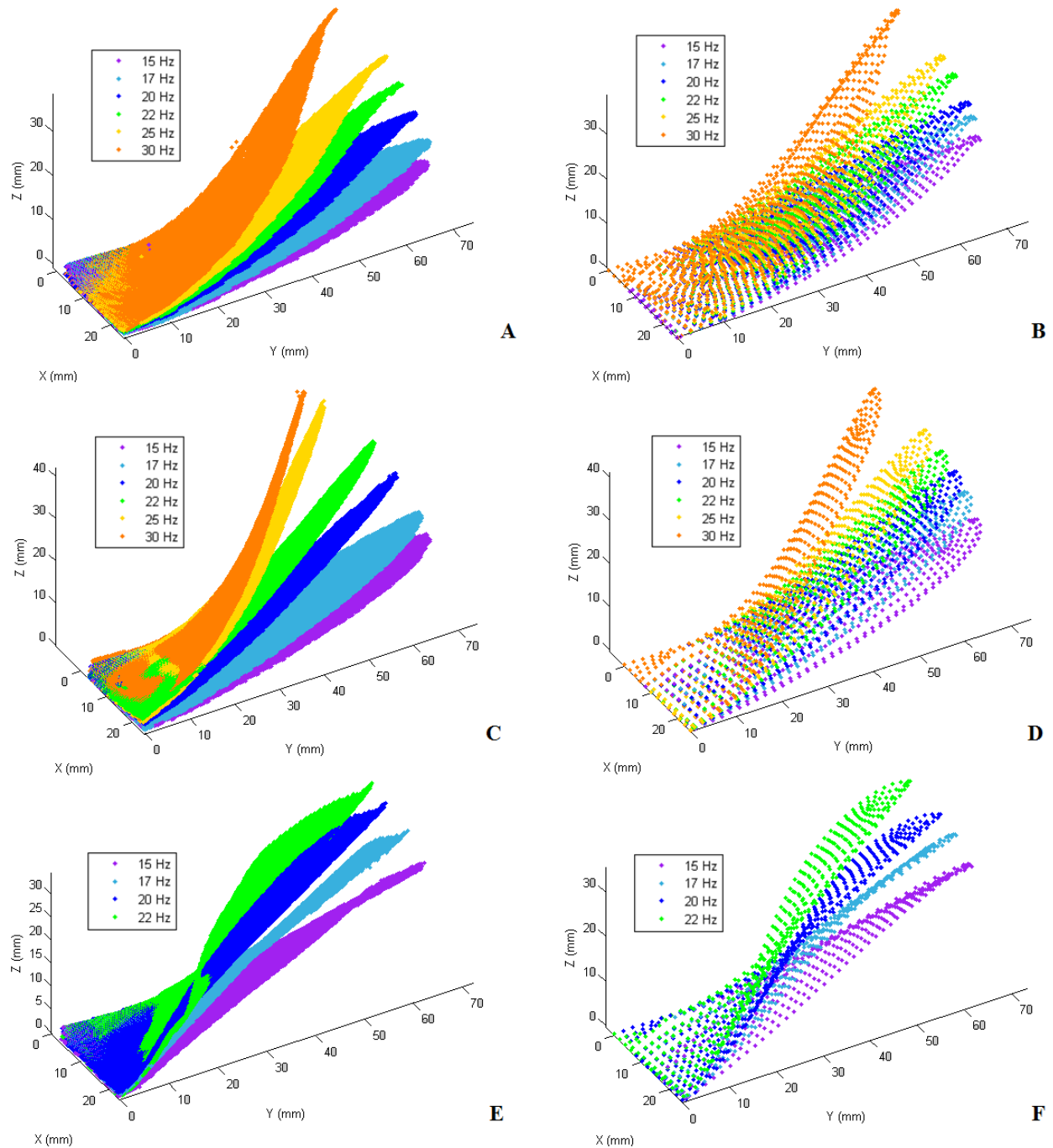


Figure 4-1. A visual comparison between the DIC images at mid-plane (left) and the model output (right). A) DIC images of Hum wing. B) Model output of Hum wing. C) DIC images of PR wing. D) Model output of PR wing. E) DIC images of Leo wing. F) Model output of Leo wing.

4.2 Tested Wing Designs

The following designs (Figure 4-2) were all tested in the Abaqus model, and their deformations were analyzed. Each wing used a different method to try and induce more twist about the leading edge. The batten structure is drawn in darker lines, while the Capran surface is lighter.

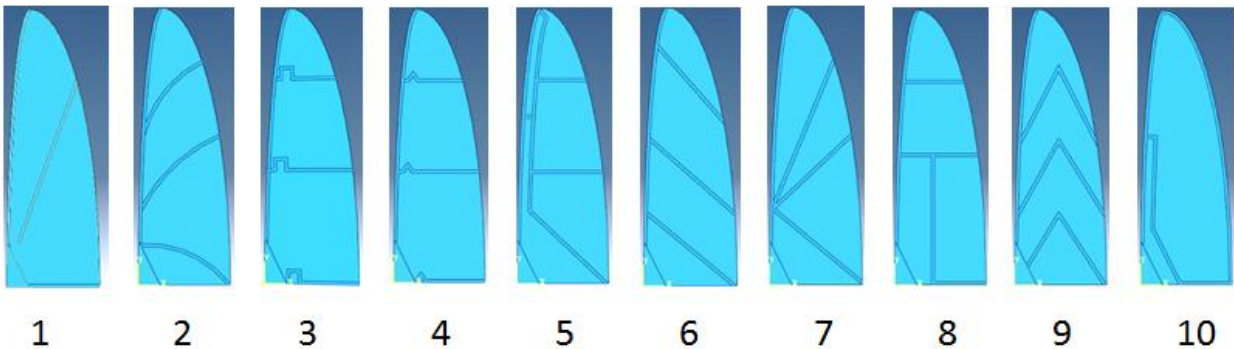


Figure 4-2. A lineup of a set of wings tested in the Abaqus code. Each wing is referred to by the wing number directly below the image of that wing.

The design choices for each of the wings were mainly exploratory, and exploited different methods to produce twisting. Wing 1 used a single, diagonal, un-attached batten to provide support, while allowing the inertia of the batten to increase twisting deformation. Wing 2 used curved battens which allowed increased bending due to the longer batten length, and the higher forces away from the root of the wing. Wings 3 and 4 utilized jogs in the battens to decrease their bending stiffness. Wing 5 used a “double leading edge”, which is essentially another batten parallel to the first leading edge, but to which the battens were attached. This allowed massive increase in twist potential. Wing 6 used diagonal battens and frees up the root deformation. Wing 7 used radial battens to concentrate the load. Wing 8 used a long jog to attach the root batten to try and elicit more deformation. Wing 9 had V shaped battens, which experienced altered

loading due to increased length and shape. Wing 10 was a new take on the standard perimeter reinforced wing, where the root batten actually attached further up on the leading edge, reducing torsional stiffness.

4.3 Model Results

All of the designs from the Section 4.2 were run through the Abaqus model, and the movement of the centroid of the twist enclosed volume was recorded. It was specifically the movement in the X and Z axis that were of interest, so instead of studying 2 graphs, a variable that encompassed both was used. This was done by

using the distance formula: $d = \sqrt{X_c^2 + Z_c^2}$

This variable was compared for each new design, and the preliminary wings that were physically tested. If a wing were to have more movement of the centroid, it was thought to possibly produce more thrust. This can be seen in Figure 4-3.

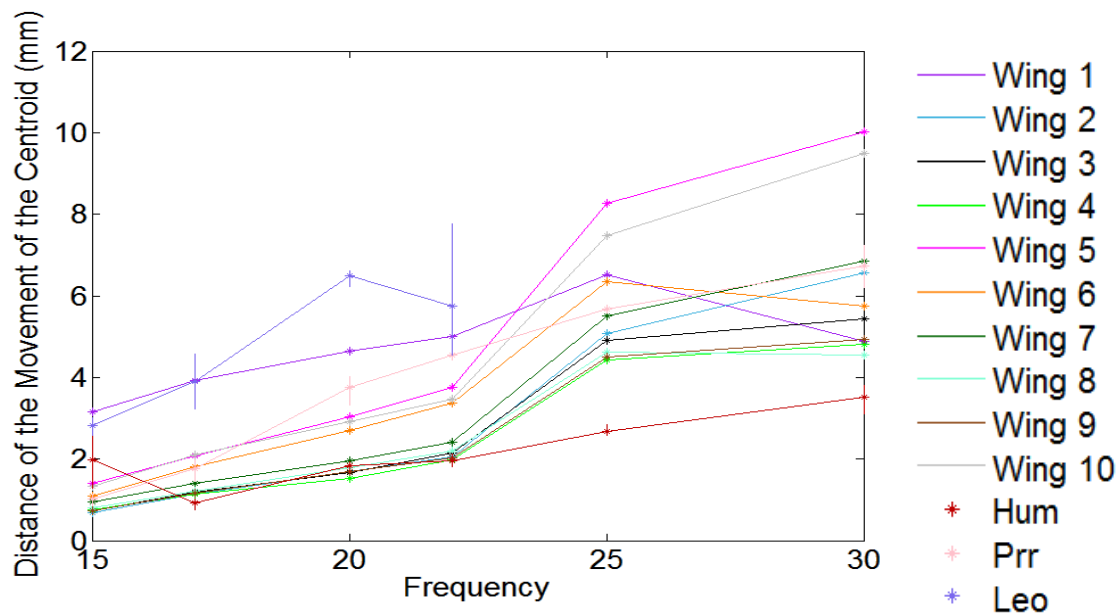


Figure 4-3. The movement of the centroid was compared for all designed wings against each other and the preliminary wings for all frequencies. The vertical lines on the graphs of the preliminary wings reflect that many values between $\pm 5^\circ$ were averaged.

As can be seen in Figure 4-3, wings 5 and 10 performed the best out of the newly designed wings. They were also tested to see if their twist enclosed volume dropped suddenly by a large amount, as this would be an indication of too much compliance. This can be seen in Figure 4-4.

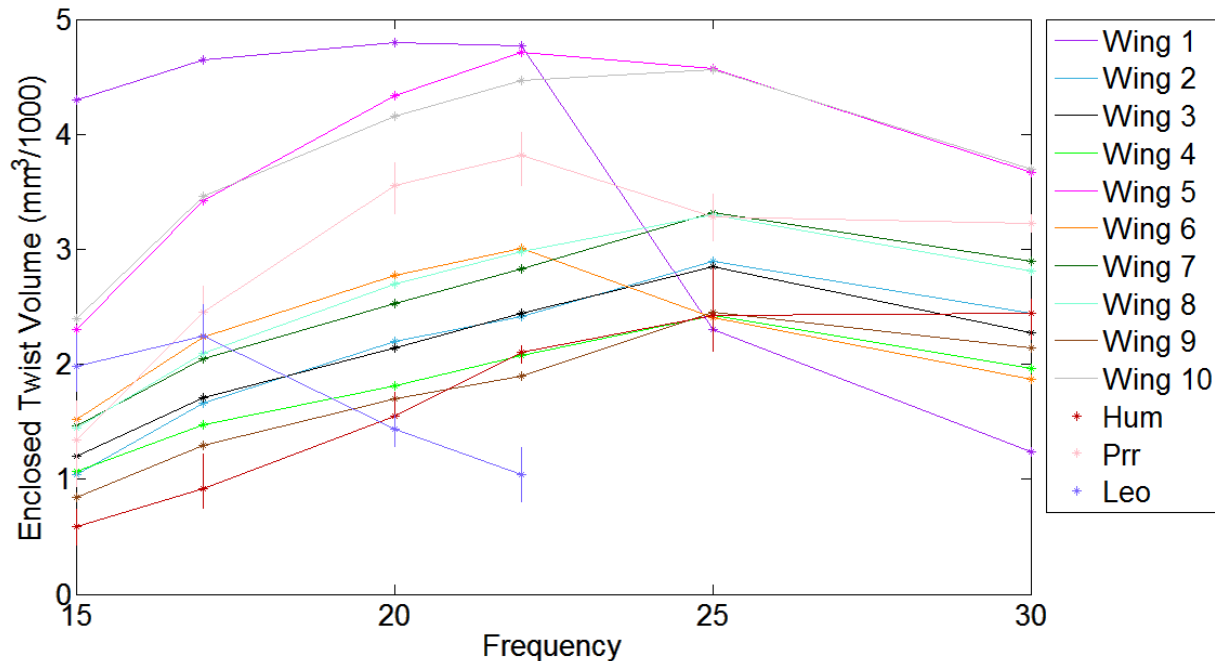


Figure 4-4. The amount of enclosed twist volume was compared for all designed wings against each other and the preliminary wings for all frequencies. The vertical lines on the graphs of the preliminary wings reflect that many values between $\pm 5^\circ$ were averaged.

It is known that the tested Leo wing failed past 22Hz, and that this may be correlated to the sudden drop in the enclosed twist volume, as seen above. Wing 1 experiences a similar trend, which indicates that it is possible that it is too flexible. While other wings, such as wings 5 and 10, do show a gradual decline, it is thought that this is rather small and is similar to the decline of the PR wing (which performed well at all frequencies). So, based on the movement of the twist centroid and the change in

twist enclosed volume, wings 5 and 10 were thought to have the most promise out of all of the new designed wings.

4.4 Build and Test of Modeled Wings

To prove the validity of the model, and the choice in selected variables, the two designs with the best performance, and the two designs with the worst performance, were fabricated and their thrust output was measured. Wing 5 and wing 10 were thought to have the ability to perform the best, and wings 8 and 9 were thought to be the worst, but it was found that nearly the opposite was true! See Figure 4-6.

Wings 5 and 10 generated significantly more thrust at 15Hz and 17Hz, but at frequencies greater than this they leveled off. This was thought to be due to too much flexibility. Because the model only simulates a single load on the wing, and does not take into account the dynamic force interaction, it was thought to have underestimated the flexibility of the wing. Other versions that were slightly stiffer than the original wing 5 and 10 architecture were manufactured and tested as well. After a few attempts, a stiffer version of wing 5 (Figure 4-5) was found to be extremely successful!

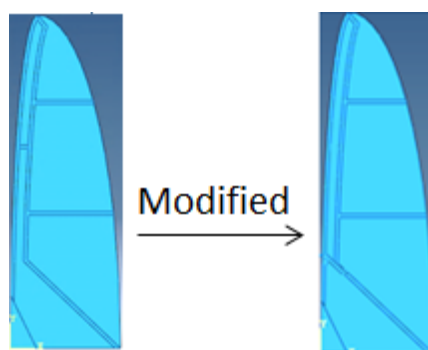


Figure 4-5. Shown above is the old wing 5, and the modification made to make it stiffer. The attachment point between the leading edge, and the second leading edge was moved towards the root of the wing, which enhanced overall stiffness.

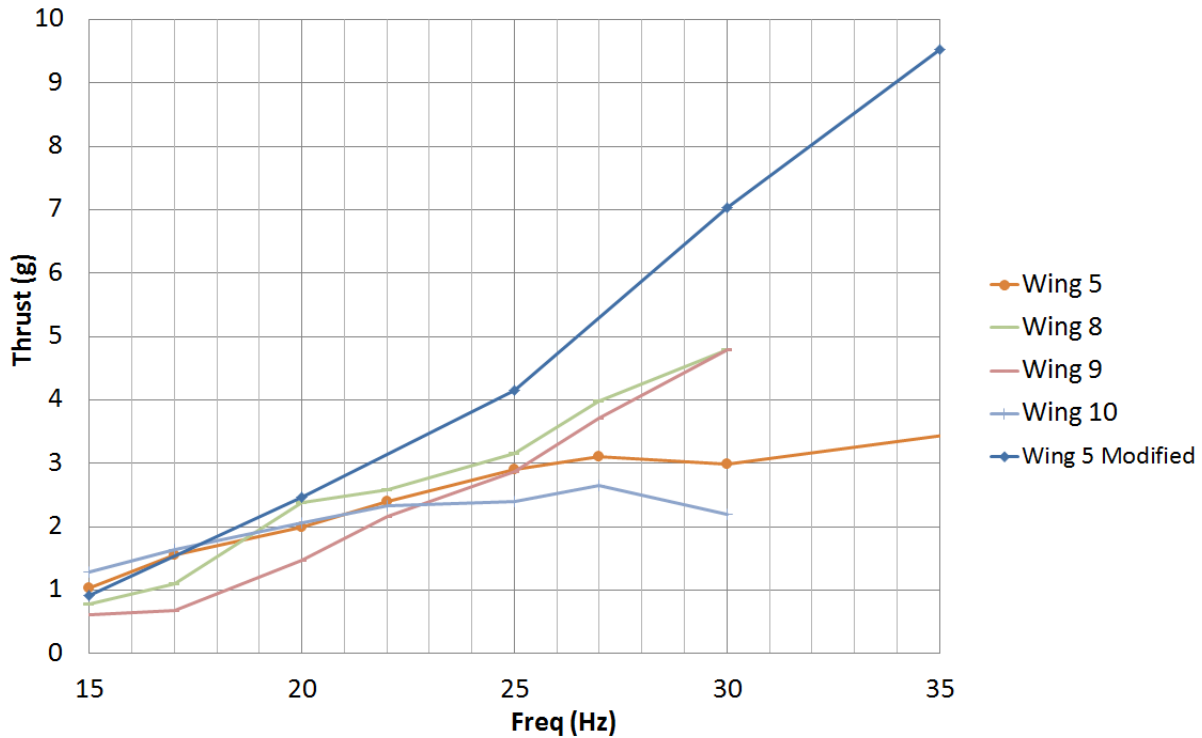


Figure 4-6. This is a graph of measured thrust vs. frequency for the 4 wings built from the model, as well as the modified wing 5. The dramatic increase in thrust production can be seen in the Wing 5 modified plot.

The modified wing 5 not only outperformed the other newly tested wings, but it outperformed the previous record holder of maximum average thrust by 18.1% at the 30Hz frequency. It can be seen at 15 Hz, that the slight increase of stiffness lowered the thrust output compared to the original wing 5, but the performance at the rest of the frequencies benefited immensely. However, the other candidate for increased thrust, wing 10, never did come to produce more thrust no matter how many iterations were attempted. This was not found to be a good design option for other reasons (Section 3.7).

CHAPTER 5 CONCLUSIONS AND FUTURE WORK

Flapping wings with multiple layouts were studied at a range of frequencies, and their net thrust and displacements were recorded. It was found through the analysis of the study, that the passive deformation of the wing during flapping could be related to the thrust output of that wing. Some other major conclusions were:

The main hypothesis that torsional compliance about the leading edge could be tailored to increase thrust potential was confirmed. It was also found that merely maximizing this could have adverse effects on flapping due to too much compliance. Furthermore, the enclosed volume and its centroid location, and more prominently the twist enclosed volume and its centroid location, could be related to the amount of twist that a wing experienced. These variables were unique in that they simplified the complexity of twisting about the leading edge into a few key measurements, which had powerful implications.

The finite element model did not necessarily find the exact architecture necessary to produce more thrust because it was a static representation of a single point in the dynamic flap cycle. It failed to simulate the inertial effects that could increase predicted deformation, and it also failed to simulate bending modes which were experienced by certain structures at varying frequencies. It was found that these modes could be witnessed using high speed cameras. Therefore it was concluded that using high speed cameras to capture the kinematics of high frequency flapping can give great insight into unforeseen complexities and phenomena.

The finite element model of the wing at mid-flap was still considered to be successful. Its ability to find designs which had the capacity to increase thrust potential,

while it minimized the time necessary to find these designs was very beneficial. It also accurately modeled the aerodynamic loading on a wing structure.

Future work should continue in the design and fabrication of wings that exhibit beneficial passive deformation, because it is in the view of the researcher that wings which generate more thrust than current models do indeed exist. A helpful parameter that could most likely be found would be if there was an optimal angle of attack for a wing in a flapping cycle. If this were found, designs which experienced too much compliance could easily be eliminated if they surpassed this value.

Although the current model was thought to be a success, the recording of the deformation of new wing architectures could help in attaining more accurate magnitudes for the loading in the finite element model. Using more data, the lambda value could be minimized, and a more true representation of what occurs in flapping could be realized. Also, the current construction method should be heavily scrutinized and updated, so that the structure of each newly constructed wing stays consistent.

It would also be beneficial for a model which simulated multiple points in the flap cycle to be used. If this were the case, the model would be able to capture both aerodynamic and inertial effects for a full range of deformations. In this way, not only can a structures' stiffness be varied, but also its mass distribution, so that its thrust potential is maximized. A tool that would help in the construction of such a model would be the use of high speed camera DIC. The use of such a system would eliminate problems due to irregular frequencies, deformation modes, and the need to organize the sequence of images.

LIST OF REFERENCES

- ¹ Sunada, S., Zeng, L., and Kawachi, K., "The Relationship Between Dragonfly Wing Structure and Torsional Deformation," *Journal of Theoretical Biology*, Vol. 193, 1998, pp. 39-45.
- ² Ennos, A. R., "The Importance of Torsion in the Design of Insect Wings," *Journal of Experimental Biology*, Vol. 140, 1998, pp. 137-160.
- ³ Combes, S. A., and Daniel, T. L., "Flexural Stiffness of Insect Wings II, Spatial Distribution and Dynamic Wing Bending," *Journal of Experimental Biology*, Vol. 206, 2003, pp. 2989-2997.
- ⁴ Sun, M., "High-lift Generation and Power Requirements of Insect Flight," *Fluid Dynamics Research*, Vol. 37, 2005, pp. 21-39.
- ⁵ Lehmann, F. O., "Aerial Locomotion in Flies and Robots: Kinematic Control and Aerodynamics of Oscillating Wings," *Arthropod Structure and Development*, Vol. 33, 2004, pp. 331-345.
- ⁶ Dickenson, M. H., "The Effects of Wing Rotation on Unsteady Aerodynamic Performance at Low Reynold's Numbers," *Journal of Experimental Biology*, Vol. 192, 1994, pp. 179-206.
- ⁷ Miao, J. M., and Ho, M. H., "Effect of Flexure on Aerodynamic Propulsive Efficiency of Flapping Flexible Airfoil," *Journal of Fluids & Structures*, Vol. 22, 2006, pp. 401-419.
- ⁸ Khan, Z. A., and Agrawal, S.K., "Force and Moment Characterization of Flapping Wings for Micro Air Vehicle Application," *American Control Conference*, WeC11.4, Portland, OR, 8-10 June 2005.
- ⁹ Chaitanya, V. K., "Design, Fabrication and Testing of an Ornithopter Wing," Department of Aerospace Engineering, Indian Institute of Technology, Mumbai, India, July 2005.
- ¹⁰ McMichael, J. M., and Francis, M.S., "Micro Air Vehicles – Towards a New Dimension in Flight," DARPA, USA, 1997.
- ¹¹ Beran, P. S., Parker, G. H., Snyder, R. D., and Blair, M., "Design Analysis Strategies for Flapping Wing Micro Air Vehicles," *Air Vehicles Directorate, Air Force Research Laboratory*, 45433-7531, Wright-Patterson AFB, OH, 2007.
- ¹² Jones, K. D., Bradshaw, C. J., Papadopoulos, J., and Platzer, M. F., "Improved Performance and Control of Flapping-Wing Propelled Micro Air Vehicles," *42nd Aerospace Sciences Meeting & Exhibit*, 2004-0399, AIAA, Reno, NV, 5-8 January 2004.

¹³Lin, C. S., Hwu, C., Young, W. B., “The Thrust and Lift of an Ornithopter’s Membrane Wings with Simple Flapping Motion,” *Aerospace Science and Technology*, Vol. 10, 2006, pp. 111-119.

¹⁴Sudo, S., Tsuyki, K., and Kanno, K., “Wing Characteristics and Flapping Behavior of Flying Insects,” *Society for Experimental Mechanics*, Vol. 45, No. 6, 2005, pp. 550-555.

¹⁵Combes, S. A., and Daniel, T. A., “Into Thin Air: Contributions of Aerodynamic and Inertial-elastic Forces to Wing Bending in the Hawkmoth *Manduca Sexta*,” *Journal of Experimental Biology*, Vol. 206, 2003, pp. 2999-3006.

¹⁶Wu, P. “Experimental Characterization, Design, Analysis, and Optimization of Flexible Flapping Wings for Micro Air Vehicles,” Ph.D. Dissertation, Department of Mechanical and Aerospace, University of Florida, Gainesville, FL, 2010.

¹⁷Beer, F. P., Johnston, E. R., and DeWolf, J. E., *Mechanics of Materials*, 4th ed., McGraw-Hill Science, New York, NY, 2009, pp. 741-742.

¹⁸Hyer, M.W., *Stress Analysis of Fiber-Reinforced Composite Materials*, Updated ed., Destech Pubns Inc., Lancaster, PA, 2009.

BIOGRAPHICAL SKETCH

Justin Daniel McIntire was born in Hollywood, Florida in 1986. He grew up in south Florida, and spent a lot of time in his father's architecture office where he learned how to draft simple floor and elevation plans, but was unsure of his career path. It wasn't until high school, after taking a course in engineering, where he finally found his true calling. He attended the University of Florida in Gainesville, and got his bachelor's degree in mechanical engineering. While obtaining his degree he worked at The Dignity Project, a non-profit organization that refurbished broken cars, which were given away to needy families. With no other prior experience, he became very proficient at automobile repair, and continues to use these skills to this day. He continued his extracurricular activities by joining the Society of Automotive Engineers, where he designed a new geared drive-train for the Baja Car that increased power transfer to the wheels. After graduating, he spent a semester at the University of Central Florida, before being accepted back to the University of Florida to obtain a Master of Science in mechanical engineering. It was never his intention to write a thesis, but after meeting with Peter Ifju, and seeing the interesting projects he worked on, he began work on just that. He extensively studied small flapping wings, and completed writing his thesis. He hopes to stay in the Gainesville area and find a job that allows him to use his education and further his experience.